Article

Discovery Medicine 2026; 38(211): 2559–2579
https://doi.org/10.24976/Discov.Med.202638211.202

Integrative Transcriptomic Analysis Identifies Glycolysis/Ferroptosis-Associated Candidate Genes in Gastric Cancer

Yongting Lan[1], Xin Zhou[1], Yongfen Ma[1], Jingmei Cao[1,*]

[1]Department of Gastroenterology, Zibo Central Hospital, 255036 Zibo, Shandong, China
*Correspondence: 18678186351@163.com (Jingmei Cao)
Submitted: 11 May 2026 Revised: 2 July 2026 Accepted: 14 July 2026 Published: 24 August 2026

Background: The crosstalk between glycolysis, ferroptosis and the gastric cancer (GC) immune microenvironment remains poorly defined. This study aims to uncover glycolysis/ferroptosis-related regulators of the GC immune microenvironment.
Methods: Transcriptomic datasets from The Cancer Genome Atlas (TCGA)-Stomach adenocarcinoma (TCGA-STAD) and Gene Expression Omnibus (GEO) were integrated to screen glycolysis/ferroptosis-related differentially expressed genes (DEGs). We evaluated univariate prognostic associations of candidate genes and built a signature for stratifying patients based on Tumor Immune Dysfunction and Exclusion (TIDE)-predicted immunotherapy response and systematically evaluated immune-related molecular signatures based on TIDE and Microsatellite Instability (MSI) scores. Single-cell RNA sequencing combined with CellChat was applied to explore cell-cell communication correlations. The oncogenic function of 5′-nucleotidase domain containing 2 (*NT5DC2*) was experimentally validated in MKN-7 GC cells and subcutaneous xenograft models.
Results: Six candidate metabolic DEGs were selected. Their individual diagnostic performance varied substantially across cohorts, although insulin-like growth factor 2 mRNA-binding protein 3 (*IGF2BP3*) and fibronectin type III domain containing 5 (*FNDC5*), together with *NT5DC2*, exhibited relatively consistent expression trends across independent datasets. Single-cell Gene Set Enrichment Analysis (GSEA) suggested a potential association between epithelial *NT5DC2* and gene signatures indicative of elevated glycolysis coupled with attenuated ferroptosis programs. Whereas B-cell *IGF2BP3* was correlated with metabolic and DNA repair gene sets. Bulk transcriptome correlation analyses indicated that elevated *NT5DC2* and IGF2BP3 expressions were associated with activated Granulin Precursor (GRN) /Transforming Growth Factor Beta 1 (TGF-β) signaling, decreased $CD8^+$ T cell abundance and T cell exhaustion signatures. Though direct functional evidence confirming this metabolic-immune regulatory axis is absent, correlative observations support its existence. A three-gene signature exhibited exploratory capacity for stratifying patients with distinct TIDE-predicted immune response profiles. Univariate survival analysis demonstrated that high *NT5DC2* expression correlated with unfavorable overall survival. This association was no longer statistically significant after adjustment for clinical covariates including age. *In vitro* and *in vivo* assays confirmed that *NT5DC2* knockdown inhibits GC proliferation and xenograft growth. The statistical significance threshold was set at $p < 0.05$.
Conclusion: We identified candidate glycolysis/ferroptosis-related biomarkers for gastric cancer. Bioinformatic correlation analyses indicated that *NT5DC2*, *FNDC5* and *IGF2BP3* expressions are associated with metabolic reprogramming signatures and predicted immunosuppressive immune phenotypes in GC.

Keywords: GC; glycolysis; ferroptosis; machine learning; immunological infiltration

Introduction

Gastric cancer (GC) is a highly malignant and heterogeneous tumor. Globally, it ranks 5th in incidence and 3nd in mortality among malignant tumors [1]. Like other malignancies, GC has a multifactorial and multistep pathogenesis. Because early clinical symptoms are often absent, most patients with GC are diagnosed at an advanced stage, when opportunities for radical resection are limited. Unfortunately, these patients frequently experience recurrence after chemotherapy [2]. Despite progress in GC treatment strategies, including intensive chemotherapy, extended surgical resection, and molecular targeted therapy, the 5-year survival rate of advanced GC patients post-surgery remains suboptimal [3]. Thus, identifying new diagnostic and therapeutic targets for GC is critical for improving its clinical management.

Metabolic reprogramming represents a core characteristic of GC occurrence and progression. Among such reprogramming events, the interaction between two phenotypes, “glycolysis” and “ferroptosis” has drawn increasing attention in recent years. As the primary metabolic pathway for tumor cells under hypoxic and nutrient-deficient conditions, glycolysis can promote glucose uptake and lactate

production via transcription factors such as HIF-1α, thereby sustaining the cells' capacity for rapid proliferation and invasion [4,5,6]. Ferroptosis is a new form of programmed cell death that is initiated by iron-dependent lipid peroxidation [7,8]. In GC, this process is critically important for preventing tumor progression and overcoming drug resistance [9,10]. Recent studies have revealed that the RON receptor tyrosine kinase triggers metabolic reprogramming in thyroid carcinoma, where RON further enhances glycolysis via the MAPK/CREB pathway. This metabolic reprogramming likely hampers ferroptosis, which could lead to chemotherapy resistance [11]. In the tumor microenvironment, lactate accumulation from increased glycolysis disrupts the redox balance, thereby limiting ferroptosis [12]. Thus, the interplay between glycolysis and ferroptosis in GC may influence metabolic adaptability, immune evasion and response to treatment. Elucidating the genetic and molecular mechanisms underlying this relationship is essential for understanding the balance between metabolism and cell death in GC.

Over the past several years, there has been increasing interest in the role of immunotherapy in GC. Immune checkpoint inhibitors (ICIs) have shown clinical benefit for a small group of patients; however, the low response rate observed in most patients remains a major concern. The principal challenge, T cell exhaustion, is the result of chronic immunosuppression and continuous exposure to tumor antigens. This condition is characterized by the loss of effector function of T cells, upregulation of inhibitory receptors, and excessive metabolic shift [13,14,15]. This leads to the progressive loss of anti-tumor immunity and reduced efficacy of ICIs [16,17]. Consequently, defining T cell dysfunction is necessary to enhance immunotherapy in GC.

Through the application of machine learning, this study prioritized a robust set of glycolysis/ferroptosis (Gly/Fer) -related transcriptomic markers within the GC landscape, ensuring rigorous selection of key differentially expressed genes. Using the combined training and validation sets, their expression patterns and phenotypic sensitivity were characterized, and key Gly/Fer-differentially expressed genes (DEGs) were identified. To quantify survival outcomes, we utilized The Cancer Genome Atlas (TCGA) -Stomach adenocarcinoma (STAD) cohort to build and verify a risk-stratification model based on the identified Gly/Fer-DEGs. By integrating single-cell transcriptome data and cell communication analysis, the potential role of these genes in $CD8^+$ T cell exhaustion was explored. In addition, we predicted the immunotherapeutic response of TCGA-STAD patients and built a corresponding prediction model based on key Gly/Fer-DEGs, providing a novel perspective for unraveling the intrinsic links among metabolism, cell death, and immune imbalance in GC and its clinical value.

Methods

Data Download and Preprocessing

First, we retrieved GC-related microarray datasets (GSE65801, GSE118916, GSE54129, GSE118897, and GSE146996) from Gene Expression Omnibus (GEO). Among them, GSE118916, GSE65801, and GSE118897 were combined as the training cohort. The intersecting genes across the three datasets were retained, and duplicate genes were averaged. Transcriptomic data underwent log2 transformation and inter-array normalization via the limma package (v3.54.0, Bioconductor project, Seattle, WA, USA). To ensure data consistency, batch effects were mitigated in the training matrix using the ComBat function from the sva package(v3.44.0, Bioconductor project, Seattle, WA, USA). For the independent validation cohorts (GSE54129 and GSE146996), duplicate gene entries were averaged. these datasets then underwent log2 transformation and normalization with normalizeBetweenArrays to produce standardized test sets. Data for the TCGA-STAD cohort were acquired from the UCSC Xena browser and used for the construction of prognostic models, evaluation of TIDE-predicted response, and validation of model expression. Detailed characteristics of the data used in the analysis can be found in Table 1. After removing cases with incomplete clinical follow-up information, 381 tumor patients were retained for multivariate Cox regression survival modeling. Genes related to ferroptosis, categorized into ferroptosis drivers, markers, and suppressors, were obtained from the FerrDb database. Genes related to glycolysis were obtained through GeneCards using the search term "glycolysis" and identified as protein-coding genes involved in glycolytic metabolism, glucose consumption, and tumor metabolic reprogramming. The full list of genes is available in **Supplementary Table 1**.

Identification of glycolysis and ferroptosis (Gly/Fer-DEGs) in GC

Using the limma package (v3.54.0), differential expression between the GC and normal tissues in the training cohort was analyzed. A linear model was applied and then specified for contrasts. Empirical Bayes moderation (eBayes) was implemented to stabilize variance estimates. To control for multiple testing, *p*-values were adjusted using the Benjamini–Hochberg false discovery rate (FDR) procedure. Genes with $|\log_2 FC| > 1$ and an adjusted p-value < 0.05 were considered DEGs.

From these DEGs, we extracted those associated with Gly/Fer-DEGs by intersecting the list with the predefined Gly/Fer gene sets. Results were visualized in a volcano plot (ggplot2 v3.4.0, R package, Winston Chang, Boston, MA, USA), where significantly up- and downregulated genes are shown in red and green, respectively. The overlap between DEGs and Gly/Fer genes was displayed using the ggvenn package (v0.1.10, R package, Yan Zhao, Beijing, China),

Table 1. Detailed information of the dataset in this study.

Data set	Database	Platform	Sample information	Cohort assignment
GSE65801	GEO	GPL14550	GC (GC = 32, Normal = 32)	
GSE118916	GEO	GPL15207	GC (GC = 15, Normal = 15)	Training set
GSE118897	GEO	GPL16686	GC (GC = 10, Normal = 10)	
GSE146996	GEO	GPL17586	GC (GC = 50, Normal = 15)	External validation set1
GSE54129	GEO	GPL570	GC (GC = 111, Normal = 21)	External validation set2
TCGA-STAD	TCGA	UCSC Xena	GC (GC = 415, Normal = 32)	Prognostic validation cohort
GSE184198	GEO	GPL24676	GC (GC = 1, Normal = 1)	Single-cell analysis

GEO, Gene Expression Omnibus; TCGA, The Cancer Genome Atlas; GC, Gastric cancer; STAD, Stomach adenocarcinoma.

and expression patterns of the identified Gly/Fer-DEGs were plotted in a heatmap utilizing pheatmap (v1.0.12, R package, Raivo Kolde, Tartu, Estonia).

Functional Enrichment Analysis of Gly/Fer-DEGs

Gene Ontology (GO) and Kyoto Encyclopedia of Genes and Genomes (KEGG) pathway analyses were carried out with the clusterProfiler package (v4.8.1, Bioconductor project, Seattle, WA, USA). Using the enrichGO function (set to "all"), we obtained terms spanning biological processes, cellular components, and molecular functions. The enrichKEGG function was applied in parallel to identify relevant metabolic and signaling pathways. Major enriched GO terms and KEGG pathways were summarized and displayed as bar plots using the visualization functions within clusterProfiler.

Machine Learning

To reduce the risk of data leakage, the integrated training cohort was assembled by merging three independent GEO datasets (GSE65801, GSE118916, and GSE118897), containing 57 gastric cancer samples and 57 normal controls (114 samples in total). Two separate independent GEO cohorts (GSE146996 and GSE54129) were used as external validation sets to assess signature generalization, while TCGA-STAD (415 gastric cancer and 32 normal samples) was applied for subsequent prognostic validation. No random subdivision of the merged GEO training cohort into internal training/internal validation subsets was performed in this study. Using expression data of the Gly/Fer-DEGs as predictors, a Least Absolute Shrinkage and Selection Operator (LASSO) classification model was fitted with the glmnet package (v4.1-8, R package, Jerome Friedman, Stanford, CA, USA). Cross-validation curves were generated after conducting ten-fold cross-validation (nfolds = 10) on training data only, which also helped in optimizing model parameters. Features with non-zero coefficients at the optimal lambda value were retained. Model performance and generalizability were subsequently assessed using the pROC (v1.18.4, R package, Xavier Robin, Montpellier, France) and rms (v6.7-0, R package, Frank Harrell, Nashville, TN, USA) packages. In Support Vector Machine-Recursive Feature Elimination (SVM-RFE) analysis, a 10-fold cross-validation framework was set up via the caret package (v6.0-94, R package, Max Kuhn, Overland Park, KS, USA) to iteratively evaluate feature importance solely based on training data. A SVM model with a radial basis kernel (method = "svmRadial") was built using the e1071 package (v1.7-13, R package, David Meyer, Vienna, Austria). Feature sizes ranging from 2 to 40 with a tuneLength of 3 were evaluated. A cross-validation error curve was plotted to determine the optimal number of feature genes and extract key genes, followed by model performance evaluation. In Random Forest (RF) analysis, an RF model containing 500 decision trees (ntree = 500) was constructed using the randomForest package (v4.7-1.1, R package, Andy Liaw, Davis, CA, USA). A ranking plot of the top 20 genes was generated using the ggpubr package (v0.6.0). Genes with an importance value greater than 1 (MeanDecreaseGini $\geq$1) were regarded as the key genes. Model performance was further evaluated using ROC analysis with the pROC package (v1.18.4, R package, Xavier Robin, Montpellier, France). In addition, calibration was assessed by a bootstrap calibration curve (method = "boot", B = 3000) generated with the rms package (v6.7-0, R package, Frank Harrell, Nashville, TN, USA), examining the agreement between predicted and observed outcomes. Genes with an importance value greater than 1 were identified as the key genes. Finally, a Venn diagram was plotted using the ggvenn package (v0.1.10, R package, Yan Zhao, Beijing, China) to identify the intersection of the key genes screened by the three models. All analyses used a random seed of 123 for reproducibility. The final selected signature was then tested on the independent validation sets to ensure unbiased performance estimation.

Expression and ROC Analysis of Key Genes

Box plots for the expression differences of key genes between normal tissues and GC tissues in the training set, validation set, and TCGA-STAD dataset were generated utilizing the ggplot2 package (v3.4.0, R package, Winston Chang, Boston, MA, USA). To explore the predictive value of key genes as biomarkers, ROC curves were first plotted using the pROC package (v1.18.4, R package, Xavier

Robin, Montpellier, France) based on the mRNA expression of the training set to verify their ability to distinguish GC samples from healthy control samples, followed by performance validation in the validation set and TCGA-STAD dataset. Considering the potential class imbalance in the validation set and TCGA-STAD dataset, weighted ROC analysis was performed during model validation, with sample weights assigned inversely proportional to the class frequencies (higher weights assigned to minority classes).

Construction of Prognostic Model

In survival analysis for prognostic modeling, the 'surv_cutpoint' function of the survival package (v3.5-5, Bioconductor project, Seattle, WA, USA) was adopted to calculate optimal cutoffs and dichotomize key gene expression into high and low subgroups. Survival objects were constructed prior to survival curve fitting with 'survfit', while the 'coxph' function was applied to calculate hazard ratios (HRs) and corresponding 95% confidence intervals. Survival curves were visualized via the 'ggsurvplot' function from the survminer package (v0.4.9, R package, Alboukadel Kassambara, Montpellier, France).

Gene Set Enrichment Analysis (GSEA) of Key Genes

To explore molecular differences between expression profiles, tumor samples in the training cohort were divided into high- and low-expression groups according to the median expression of key genes. Differential expressions between groups was identified utilizing the limma package (v3.54.0, Bioconductor project, Seattle, WA, USA, $p < 0.05$). GSEA was then conducted using clusterProfiler (v4.8.1, Bioconductor project, Seattle, WA, USA) against the Hallmark gene set (h.all.v2023.1.Hs.symbols.gmt), with significance set at $p < 0.05$. Enriched pathways were visualized as GSEA curves using the gseaplot2 function from enrichplot (v1.20.0, Bioconductor project, Seattle, WA, USA).

Immune Cell Infiltration Analysis

Tumor purity was assessed with the estimate package (v1.0.13, Bioconductor project, Seattle, WA, USA). Differences in ImmuneScore, StromalScore, and Estimation of STromal and Immune cells in MAlignant Tumor tissues using Expression data (ESTIMATE) scores between groups were plotted with ggpubr (v0.6.0, R package, Alboukadel Kassambara, Montpellier, France). Missing purity values were imputed via linear regression. The relative abundance of 22 immune cell types was determined using the Cell-type Identification by Estimating Relative Subsets of RNA Transcripts (CIBERSORT) algorithm (Stanford University, Stanford, CA, USA) with 1000 permutations, and samples were filtered for FDR-adjusted $p < 0.05$. To the greatest extent possible, CIBERSORT scores were adjusted for tumor purity before correlation analyses. Heatmaps were used to visualize differences in immune infiltration between tumor and normal tissues, while violin plots and correlation bubble charts were used to analyze the association between subsets of immune cells and gene expression.

Single-Cell Data Processing

All analyses were performed using R (v4.0.1, R Foundation for Statistical Computing, Vienna, Austria). The quality control steps resulted in a final count of 2956 normal gastric cells and 3623 tumor cells. Cells were filtered based on nFeature_RNA between 200 and 2500 and <5% mitochondrial gene content. Batch effects were corrected utilizing Harmony (v0.1.0, R package, Ilya Korsunsky, Boston, MA, USA). Dimensionality reduction was performed using Principal Component Analysis (PCA) (with the top 15 components) followed by t-distributed Stochastic Neighbor Embedding (t-SNE). Cell types were annotated based on established marker genes in combination with the CellMarker database and were further refined manually. The visualization of highly variable genes was achieved utilizing dot plots, and dropout effects were minimized by applying expression smoothing with MAGIC (v3.0, Python toolkit, Dana Pe'er Lab, New York, NY, USA). Patterns and distribution of gene expression were depicted with ggplot2 and Nebulosa(v1.0.1, R package, Jose Alquicira Hernandez, Austin, TX, USA).

In this study, the use of Cell-Cell Communication (CellChat, v1.1.3, R package, Suoqin Jin, Los Angeles, CA, USA) involved analyzing cellular communication. Potential ligand–receptor pairs were determined after the CellChat object was built from normalized data and cell labels. Communication probability and pathway activity were inferred and integrated into a global signaling network. Heatmaps were used to assess differences between normal and tumor groups, whereas bubble and circle plots were used to depict interaction patterns between cell types. The signaling functions of epithelial and B cells were investigated using network-based methods. Sankey diagrams provided an overview of signaling, focusing on the most significant pathways. The expression of selected ligand–receptor pairs and correlations among hub genes were visualized accordingly.

TIDE-Predicted Response Prediction and Modeling

TIDE-predicted response was estimated using the TIDE algorithm based on TCGA-STAD data. Associations between gene expression and immunotherapy-related markers were assessed using Spearman correlation and visualized as a heatmap. Patients were stratified into responder and non-responder groups, and survival differences were analyzed using the log-rank test via survival package (v3.5-5, Bioconductor project, Seattle, WA, USA). A logistic regression model including fibronectin type III domain containing 5 (FNDC5), NT5DC2, and insulin-like growth factor 2 mRNA-binding protein 3 (IGF2BP3) was constructed. Model performance was evaluated using ROC

analysis, with AUC as the main metric, and calibration was assessed using bootstrap-based calibration curves. Finally, multivariate results were summarized as odds ratios with 95% confidence intervals and presented in a forest plot via forestmodel (v0.5.0, R package, Nick Kennedy, London, UK).

Cell Culture

GES-1 and MKN-7 cells (Procell, CL-0563 and CL-0574, Wuhan, China) were maintained in RPMI-1640 (Procell, PM150110, Wuhan, China) supplemented with 10% FBS (Gibco, 10099141, Grand Island, NY, USA) and 1% penicillin-streptomycin (Meilunbio, MA0110, Dalian, China) at 37 °C with 5% CO_2. All cell lines were authenticated by short tandem repeat (STR) profiling and confirmed to be free of mycoplasma contamination before use.

Quantitative Real-Time Polymerase Chain Reaction (qPCR) Analysis

Total RNA was extracted with TRIzol reagent (CWBI, CW0581M, Beijing, China), followed by reverse transcription using the Evo M-MLV RT Master Mix (Accurate Biology, AG11706, Changsha, China). qPCR was performed with SYBR Green Pro Taq HS Premix (Accurate Biology, AG11701, Changsha, China), using Glyceraldehyde-3-Phosphate Dehydrogenase (GAPDH) as the internal control. The $2^{-\Delta\Delta Ct}$ relative quantification method was adopted to calculate the relative mRNA expression levels. The cycling conditions included an initial denaturation at 95 °C for 30 s, followed by 40 cycles of 95 °C for 5 s and 60 °C for 30 s. Primer sequences: NT5DC2 F: 5′-GTGGCTTCTATGGCAAGGGT-3′, R: 5′-TTCACATGCACGTCTCGGAT-3′; GAPDH F: 5′-AGAAGGCTGGGGCTCATTTG-3′, R: 5′-GGGGCCATCCACAGTCTTC-3′.

Western Blotting

Proteins were separated on 10% Sodium Dodecyl Sulfate-Polyacrylamide Gel Electrophoresis (SDS-PAGE) gels (Boster, AR0138, Wuhan, China) and transferred onto Polyvinylidene Difluoride (PVDF) membranes (Millipore, IPVH00010, Burlington, MA, USA) at 200 mA for 60 min. The membranes were then incubated with primary antibodies against NT5DC2 (1:3000, Proteintech, 31739-1-AP, Wuhan, China) and GAPDH (1:10,000, Proteintech, 60004-1-Ig, Wuhan, China), followed by Horseradish Peroxidase (HRP)-conjugated secondary antibodies (1:10,000, ZSGB-BIO, ZB-2301/ZB-2305, Beijing, China). Protein bands were detected using Enhanced Chemiluminescence (ECL) reagents (Meilunbio, MA0186-1, Dalian, China). ImageJ software was used to measure the integrated optical density (IOD) of each band; the relative protein expression of target genes was normalized to the IOD of the internal reference GAPDH band.

Cell Transfection

For transient knockdown, cells were transfected with synthetic small interfering RNAs (siRNAs), including si-NT5DC2 (si-1, sense: 5′-GCGUGGACUUCACCUUCUACC-3′, antisense: 5′-UAGAAGGUGAAGUCCACGCGG-3′; si-2, sense: 5′-AGCUGUUCCUCAUCACCAACA-3′, antisense: 5′-UUGGUGAUGAGGAACAGCUGU-3′) or a negative control siRNA (si-NC, sense: 5′-UUCUCCGAACGUGUCACGUTT-3′, antisense: 5′-ACGUGACACGUUCGGAGAATT-3′). Briefly, 100 pmol siRNA and 6 µL Lipofectamine 2000 (Invitrogen, 11668-019, Carlsbad, CA, USA) were diluted in Opti-MEM (Yuchun, YC-3039A, Shanghai, China), incubated for 20 min at room temperature, and then added to cells cultured in RPMI-1640. The culture medium was replaced with fresh complete medium 5 h post-transfection, and the knockdown efficiency was evaluated using qPCR at 30 h.

For stable knockdown, MKN-7 cells were transfected with shRNA plasmids targeting NT5DC2 (sh-1, target sequence: 5′-TGGCAAGGGTCCCTCCATTAA-3′; sh-2, target sequence: 5′-TCCGCTGAGGGCACCTTTATT-3′; sh-3, 5′-TCCACCCAGACAAGCAATAAA-3′) or a negative control plasmid (sh-NC, sequence: 5′-TTCTCCGAACGTGTCACGTTT-3′) using Lipofectamine 2000 according to a similar protocol, with 2 µg of plasmid DNA used per well in a 6-well plate. The medium was likewise refreshed after 5 h. At 48 h post-transfection, cells were subjected to continuous selection in complete medium supplemented with 2 µg/mL puromycin for 14 days to eliminate untransfected cells. Surviving single-cell clones were isolated, expanded, and verified via qPCR to select clones with stable and optimal NT5DC2 knockdown for subsequent *in vivo* xenograft assays.

To ensure persistent gene silencing throughout the animal studies, NT5DC2 expression was verified by qPCR in the stable cell suspensions immediately prior to subcutaneous injection.

Cell Viability Assay

Cell viability after 0, 24, 48, 72, and 96 hours was assessed using the Cell Counting Kit-8 assay (Beyotime, C0039, Shanghai, China). We seeded 2×10^3 cells per well in 96-well plates with 100 µL complete medium per well. After adding 10 µL of the reagent to each well and incubating for 1 h, the absorbance was measured at 450 nm.

Cell Migration Assay

Cell migration was assessed using Transwell inserts (8 µm; Falcon, 353097, Corning, NY, USA). Transfected cells (3×10^4 per well) in serum-free medium were added to the upper chamber, and medium containing 30% FBS (Gibco, Grand Island, NY, USA) was added to the lower chamber. After 24 h, the cells that had migrated were fixed, stained with Crystal Violet (Solarbio, G1063, Beijing, China), and

counted under a microscope (200×). Three random non-overlapping visual fields were selected for each well, and the average cell count of the three fields was recorded as the migration cell number of the well.

Apoptosis Analysis by Flow Cytometry

After transfection, MKN-7 cells were harvested at 30 h, treated with PBS (Servicebio, G4202, Wuhan, China), and then stained with Annexin V-PE/7-AAD (Meilunbio, MA0429, Dalian, China) for 15 min in the dark at room temperature. Samples were analyzed on a BD FACSVerse flow cytometer. Unstained cells, Annexin V single-stained and 7-AAD single-stained control groups were prepared to calibrate instrument voltages and set quadrant gating thresholds. FSC/SSC scatter plots were first applied to isolate intact single cells and remove cell debris, followed by calibrated PE/7-AAD two-dimensional plots to categorize cell subgroups. The total apoptosis rate was calculated as the sum of early apoptotic cells (Q3-4, Annexin V^+/7-AAD^-) and late apoptotic cells (Q3-2, Annexin V^+/7-AAD^+).

Tumor Xenograft Experiment

As for the animal experiments, ethical approval was granted by the Ethics Committee of Zibo Central Hospital (Approval No. 202211008). The study used female BALB/c nude mice (4–6 weeks old, 20–25 g) from Jinan Xingkang Biotechnology Co., Ltd. The mice were assigned into 2 groups (n = 4/per group): sh-NT5DC2 and sh-NC. Each mouse was inoculated subcutaneously with 1×10^6 transfected MKN-7 cells on the right flank. Tumor volume was calculated using the formula: V (mm^3) = (length × $width^2$) / 2. After 27 days of tumor observation, mice were humanely euthanized with 5% isoflurane in oxygen (1 L/min). After breathing ceased for at least one minute, cervical dislocation was performed to confirm death prior to tumor harvest, weighing and photography. Tumor tissues were fixed for subsequent hematoxylin and eosin (H&E) staining and immunohistochemical (IHC) staining. All procedures complied with the ARRIVE Guidelines 2.0.

H&E Staining

Harvested xenograft tumor tissues were fixed in 4% paraformaldehyde for 24 h, followed by graded ethanol dehydration and paraffin embedding. Tissue blocks were cut into 4 μm sections. After xylene dewaxing and hydration, sections were subjected to routine H&E staining and morphological observation under optical microscopy.

IHC Staining

Paraffin slices (4 μm) underwent standard dewaxing and antigen retrieval. After blocking, sections were incubated with anti-Ki67 primary antibody (1:200, ab16667, Abcam, Cambridge, UK) overnight at 4 °C, followed by HRP-conjugated secondary antibody (1:200, ab214880, Abcam, Cambridge, UK) incubation at room temperature for 60 min. 3,3′-Diaminobenzidine (DAB) was applied for chromogenic reaction, and hematoxylin was used for nuclear counterstaining prior to microscopic examination. At the same time, we used the plus IHC Profiler plugin module in ImageJ software to conduct quantitative analysis of immunohistochemical images to calculate Ki67 positive cell ratios for statistical comparison [18].

Statistical Analysis

Data were analyzed in R (v4.0.1, R Foundation for Statistical Computing, Vienna, Austria). After normalization and preprocessing, two-group comparisons were performed using Student's *t*-test, and multiple-group comparisons were conducted with one-way ANOVA. For survival analyses, the Kaplan–Meier method with the log-rank test was applied, and Cox proportional hazards regression models were used to evaluate prognostic factors. Associations between gene expression and immune infiltration or clinical characteristics were determined using correlation analysis, as appropriate. Shapiro-Wilk test was used to judge normal distribution. Normally distributed data adopted Student's *t*-test/ANOVA, while non-normal data applied Wilcoxon and Kruskal-Wallis tests. Unless otherwise specified, a two-sided $p < 0.05$ was considered statistically significant.

Results

Identification of Gly/Fer-Related Genes in GC

To investigate the role of Gly/Fer in GC, GSE65801, GSE118916, and GSE118897 were combined as the training set, whereas GSE54129 and GSE146996, which have larger sample sizes, were used as independent validation cohorts. In the training set, 681 DEGs were identified using the thresholds adj.*p*.Val < 0.05 and |logFC| >1, and visualized by a volcano plot (Fig. 1A). Intersection analysis with Gly/Fer-related gene sets yielded 29 Gly/Fer-DEGs, including 15 upregulated and 14 downregulated genes (Fig. 1B, **Supplementary Table 2**), with expression patterns shown in a heatmap (Fig. 1C).

Functional enrichment analysis indicated that these genes were mainly involved in cholesterol metabolism, mineral absorption, HIF-1 signaling, pluripotency regulation, nitrogen metabolism, and cellular senescence pathways (Fig. 1D), implying their involvement in metabolic reprogramming, oxidative stress response, stemness maintenance and cell cycle regulation. GO enrichment further supported their functions at multiple levels (Fig. 1E). For biological processes, these genes were closely related to plasma lipoprotein particle clearance, hypoxia response, and metabolic stress. At the cellular component level, they were enriched in chylomicrons, very-low-density lipoprotein particles and protein–lipid complexes. Significant enrichment was observed in molecular functions related to growth factor receptor binding and protein kinase B (AKT)

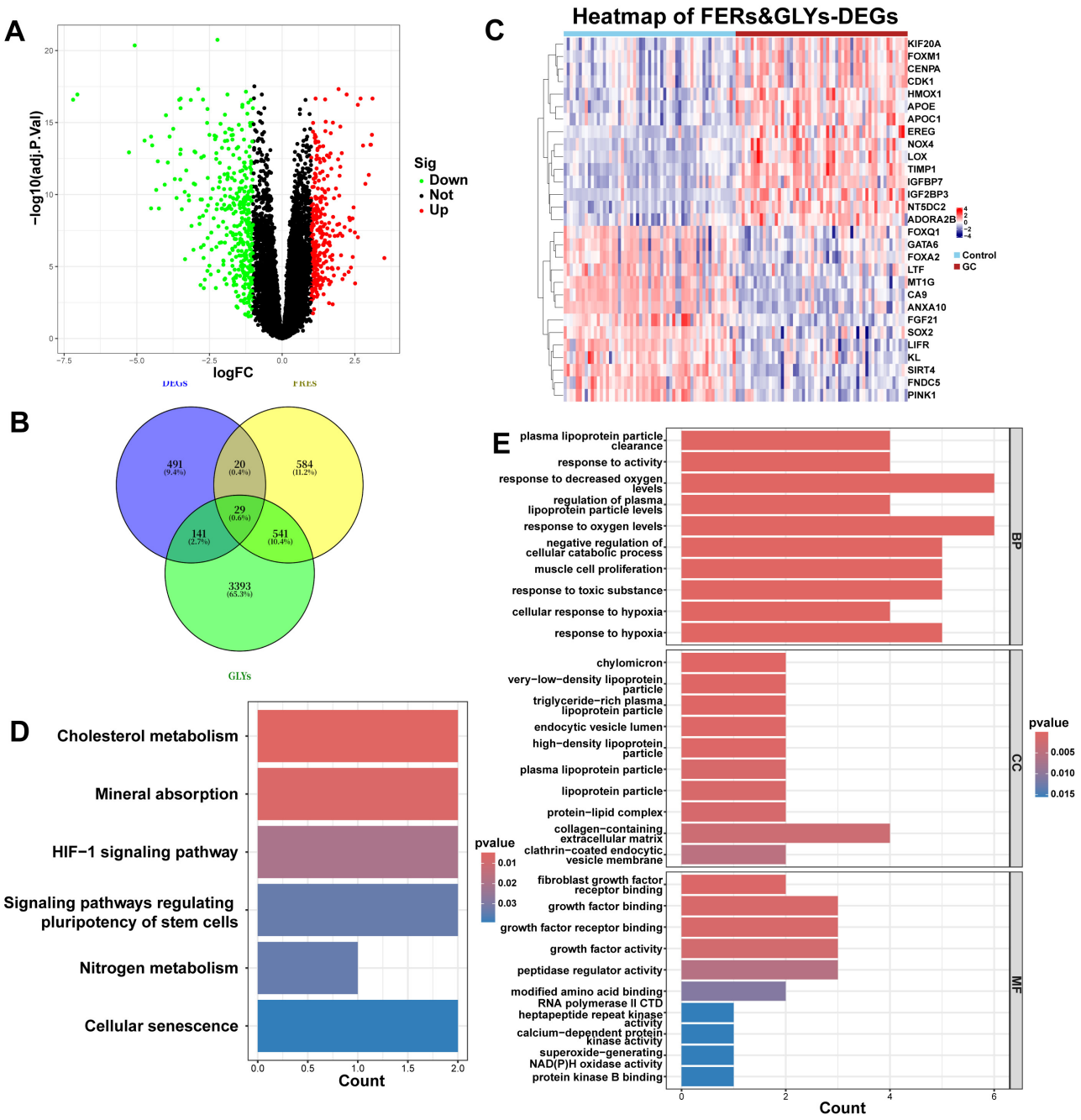

Fig. 1. Identification and functional characterization of glycolysis/ferroptosis-related differentially expressed genes (Gly/Fer-DEGs) in gastric cancer (GC). (A) Volcano plot of all genes. (B) Venn diagram showing the intersection between Gly/Fer-related genes and DEGs. (C) Heatmap of the Gly/Fer-DEGs differentially expressed in GC. (D) Kyoto Encyclopedia of Genes and Genomes (KEGG) pathway enrichment analysis of Gly/Fer-DEGs. (E) Gene Ontology (GO) enrichment analysis of Gly/Fer-DEGs.

binding. These metabolic processes, stress responses, lipid transport, and signaling pathways involved in intracellular communication.

Identification of Core Gly/Fer-DEGs

For hub gene identification, a combination of three machine-learning techniques was employed. In the random forest model, classification error was stable when the number of trees reached approximately 500 (Fig. 2A). From this model, 16 genes were identified with importance scores >1 (Fig. 2B). Both the calibration and ROC analyses in the training cohort demonstrated a good predictive performance, with an AUC of 0.964 (Fig. 2C,D). Using the penalty and coefficient curves, LASSO regression identified 12 candidate genes (Fig. 2E,F), and the model showed an AUC of 0.993, indicating a good performance (Fig. 2G,H). The SVM-RFE algorithm identified 8 optimal feature genes (Fig. 2I) with classification efficiency, with

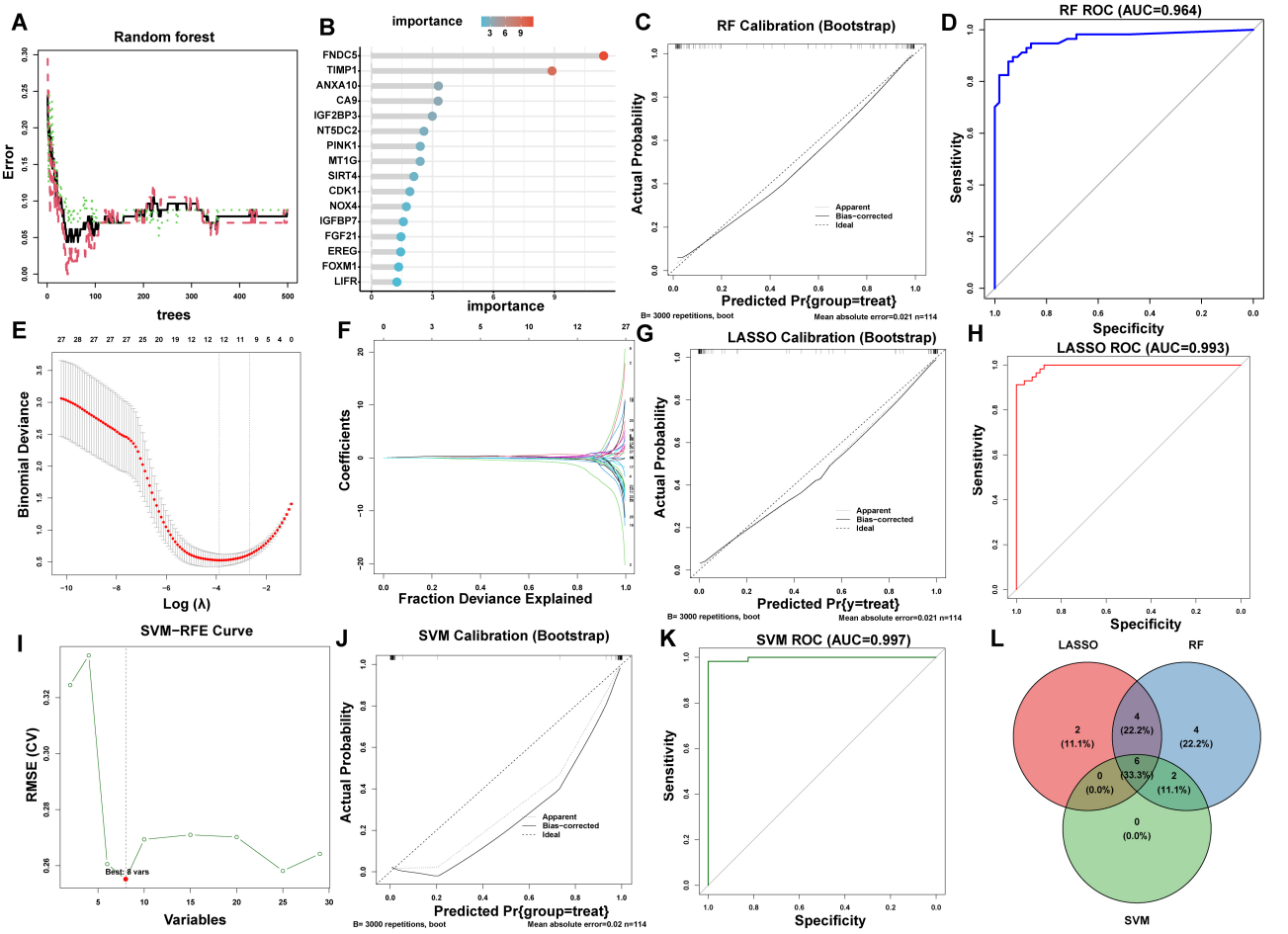

Fig. 2. Machine learning-based identification of key genes in GC. Candidate genes were selected using (A) an error plot of the Random Forest model. (B) Importance lollipop plot of genes with importance >1 in the RF model (16 key genes). (C) Calibration curve of the RF model. (D) ROC analysis plot of the RF model (AUC = 0.964). (E) LASSO bias-penalty parameter plot. (F) LASSO coefficient-proportion of variance explained plot (12 key genes). (G) Calibration curve of the LASSO model. (H) ROC analysis plot of the LASSO model (AUC = 0.993). (I) RMSE-variable count relationship plot of SVM (8 key genes). (J) Calibration curve of the SVM model. (K) ROC analysis plot of the SVM model (AUC = 0.997). (L) Venn diagram displaying the six overlapping key genes identified across all three algorithms. RF, Random Forest; ROC, Receiver Operating Characteristic; LASSO, Least Absolute Shrinkage and Selection Operator; AUC, Area Under the Curve; RMSE, Root Mean Square Error; SVM, Support Vector Machine.

an AUC of 0.997 (Fig. 2J,K). Finally, six stable core genes (*CA9*, *FNDC5*, *IGF2BP3*, *MT1G*, *NT5DC2*, and *SIRT4*) were obtained by intersecting the three gene sets (Fig. 2L), supporting their critical roles in modulating glycolysis and ferroptosis in gastric cancer.

Expression Patterns and ROC Analysis of Key Gly/Fer-DEGs

To further prioritize the clinically relevant candidate biomarkers, we performed a comprehensive survival analysis of the six previously identified key genes, including *CA9*, *FNDC5*, *IGF2BP3*, *MT1G*, *NT5DC2*, and *SIRT4*. Based on the log-rank test in the TCGA-STAD cohort, only *FNDC5*, *IGF2BP3*, and *NT5DC2* exhibited a statistically significant association with patient survival ($p < 0.05$). As shown in Fig. 3A–D, the expression levels of *CA9*, *FNDC5*, *MT1G*, and *SIRT4* generally showed a downward trend in the training set and TCGA-STAD cohort, while *IGF2BP3* and *NT5DC2* showed an upward trend. However, no significant difference was observed for SIRT4 in the validation set GSE146996, for MT1G in the validation set GSE54129, or for *CA9* in the TCGA-STAD cohort. Fig. 3E–H present ROC curves of individual hub genes for distinguishing gastric cancer from normal tissues. In the training cohort, NT5DC2 (AUC = 0.906), SIRT4 (AUC = 0.901), CA9 (AUC = 0.880), IGF2BP3 (AUC = 0.902), FNDC5 (AUC = 0.871), and MT1G (AUC = 0.849) exhibited relatively high AUC values. Weighted ROC analysis was applied in three external cohorts to offset sample size imbalance between tumor and normal groups. In GSE146996, the AUCs were 0.820 for NT5DC2, 0.593 for SIRT4, 0.859 for CA9, 0.764 for IGF2BP3, 0.741 for

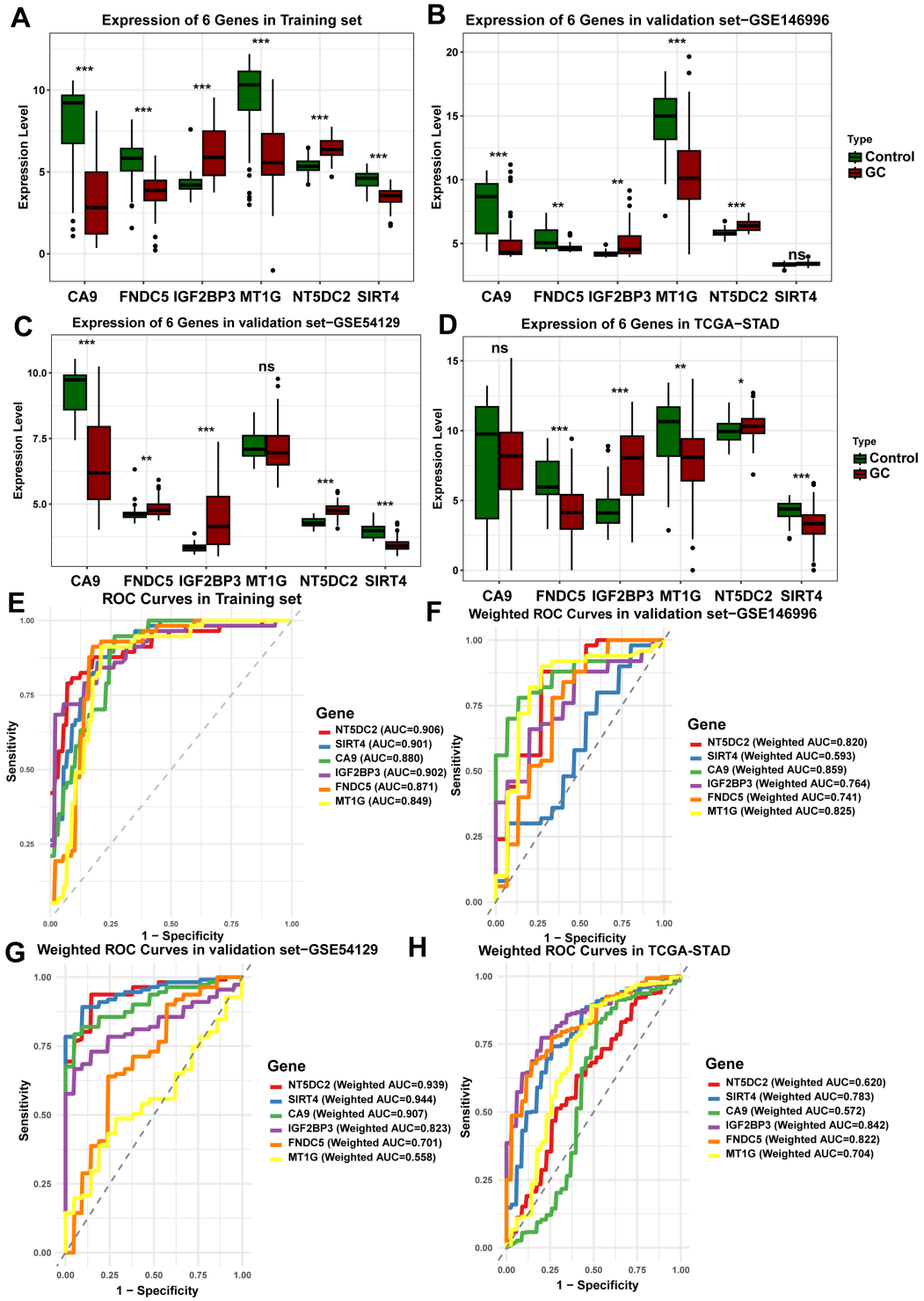

Fig. 3. Expression patterns and ROC analysis of key Gly/Fer-DEGs. (A–D) Expression levels of *CA9*, *FNDC5*, *IGF2BP3*, *MT1G*, *NT5DC2*, and *SIRT4* in GC analyzed across the training set, validation set, and TCGA-STAD dataset. (E–H) ROC curves of *CA9*, *FNDC5*, *IGF2BP3*, *MT1G*, *NT5DC2*, and *SIRT4* in GC analyzed across the training set, validation set, and TCGA-STAD dataset. *$p < 0.05$, **$p < 0.01$, ***$p < 0.001$, ns, not significant. Gly/Fer, glycolysis/ferroptosis; DEGs, differentially expressed genes; CA9, Carbonic Anhydrase 9; FNDC5, fibronectin type III domain containing 5; IGF2BP3, insulin-like growth factor 2 mRNA-binding protein 3; MT1G, Metallothionein 1G; NT5DC2, 5′-nucleotidase domain containing 2; SIRT4, Sirtuin 4; TCGA, The Cancer Genome Atlas; STAD, Stomach adenocarcinoma.

FNDC5, and 0.825 for MT1G. In GSE54129, the corresponding AUCs were 0.939, 0.944, 0.907, 0.823, 0.701, and 0.558, respectively. In the TCGA-STAD cohort, the AUCs were 0.620 for *NT5DC2*, 0.783 for *SIRT4*, 0.572 for *CA9*, 0.842 for *IGF2BP3*, 0.822 for *FNDC5*, and 0.704 for *MT1G*. Notably, several genes yielded AUC values near the random classification threshold (AUC = 0.5) in certain validation sets. *SIRT4* scored 0.593 in GSE146996, *MT1G* scored 0.558 in GSE54129, and *CA9* scored 0.572 in TCGA-STAD. These results reflected limited discriminative power of these genes in specific patient populations. Overall, the six Gly/Fer-related DEGs exhibited inconsistent diagnostic performance across independent datasets. Only *NT5DC2*, *IGF2BP3* and *FNDC5* exhibited moderate discriminatory performance across most cohorts. The remaining genes showed unstable predictive performance and were therefore unlikely to serve as reliable standalone diagnostic markers.

Exploratory Prognostic Association Analysis of Candidate Genes

High expression levels of *FNDC5*, *IGF2BP3*, and *NT5DC2* were significantly associated with poorer overall survival (OS) of patients in the TCGA-STAD cohort in univariate survival analysis, suggesting that these genes have potential prognostic correlation with GC outcomes (Fig. 4A–C). The multivariate Cox regression forest plot including all available clinical covariates (*NT5DC2*, tumor stage, age, gender) is presented in Fig. 4D. In this fully adjusted model, NT5DC2 no longer reached conventional statistical significance (HR = 1.20, 95% CI 0.98–1.48, $p = 0.080$), while advanced tumor stage and older age remained independent adverse prognostic factors. Prior to Cox regression modeling, all patients with incomplete clinical metadata were excluded, leaving a total of 381 eligible TCGA-STAD samples for this multivariate survival analysis. Stage II presented a marginal elevated risk trend ($p = 0.149$, HR = 1.63, 95% CI = 0.84–3.15). Stage III–IV correlated with significantly worse overall survival ($p < 0.001$, HR = 3.08, 95% CI = 1.68–5.65). Increasing age also independently predicted worse survival outcome (HR = 1.03, 95% CI 1.01–1.04, $p = 0.003$). Gender had no significant prognostic effect. Collectively, univariate survival analyses confirmed elevated expression of the three genes correlates with worse GC prognosis. Nevertheless, *NT5DC2* cannot be defined as an independent prognostic biomarker after full adjustment of major clinical confounders including age.

Association of Key Genes With Immune Infiltration in Gastric Cancer

ESTIMATE analysis showed higher ImmuneScore, StromalScore, and ESTIMATEScore in GC tissues, together with reduced tumor purity compared with normal samples (Fig. 5A, $p < 0.05$), indicating increased stromal and immune components.

After filtering for quality (33 normal and 34 GC samples), the immune cell composition analysis showed marked variability between samples (Fig. 5B). Correlation analysis was conducted after adjusting for tumor purity. A full correlation matrix was subsequently analyzed. In the normal group, several immune cell subtypes were correlated. Specifically, there was a correlation between memory B cells and $CD4^+$ T cells, as well as between dendritic cells and mast cells (Fig. 5C). This pattern was not observed in the GC tissues. In GC samples, Tregs and γδ T cells were positively correlated ($r = 0.65$, $p < 0.001$). Additionally, M0 macrophages and neutrophils were also positively correlated ($r = 0.55$, $p < 0.01$) (Fig. 5D).

The group comparisons demonstrated distinct differences in immune composition (Fig. 5E). In GC, plasma cells, $CD8^+$ T cells, and resting NK cells were decreased, whereas Tregs, γδ T cells, activated NK cells, and M0/M1 macrophages were increased.

The relationship between key genes and immune infiltration was further examined. *NT5DC2* expression showed a weak negative correlation with $CD8^+$ T cells (Fig. 5F, $p < 0.05$). *IGF2BP3* was negatively associated with plasma cells (Fig. 5G, $p < 0.05$). *FNDC5* showed a significant negative correlation with T follicular helper cells ($r < 0$, $p < 0.001$) and was also related to Tregs, mast cells, and M0 macrophages (Fig. 5H, $r < 0$, $p < 0.05$).

Expression Patterns of FNDC5, NT5DC2, and IGF2BP3 in GC Single-Cell Data

In this single-patient exploratory dataset, t-SNE dimensionality reduction was first used to visualize cell distributions derived from one normal gastric sample and one gastric cancer sample. A total of 11 major cell populations were annotated, including B cells, $CD4^+$ T cells, effector $CD8^+$ T cells, epithelial cells, exhausted CD8 T cells, macrophages, monocytes, neutrophils, plasma cells, stem cells, and tissue-resident memory $CD8^+$ T cells (Fig. 6A). The bubble plot of highly variable genes further outlined characteristic molecular markers for each cell subtype (Fig. 6B). Gene expression density mapping across cell clusters indicated *FNDC5* predominantly localized to stem cell populations, *NT5DC2* concentrated within epithelial cell clusters, and *IGF2BP3* primarily distributed in B cell subsets (Fig. 6C). MAGIC imputation was applied to mitigate sparsity inherent to single-cell transcriptomic data, and expression comparisons were carried out on the imputed matrix. Broad expression trends across all captured cells suggested relatively lower *FNDC5* abundance and relatively higher *NT5DC2* and *IGF2BP3* levels in tumor-derived cells relative to normal gastric cells (Fig. 6D). Cell-type-restricted expression profiling further revealed a trend of reduced *FNDC5* signals in stem cell clusters, elevated *NT5DC2* expression within epithelial populations, and increased *IGF2BP3* abundance in B cell subsets (Fig. 6E).

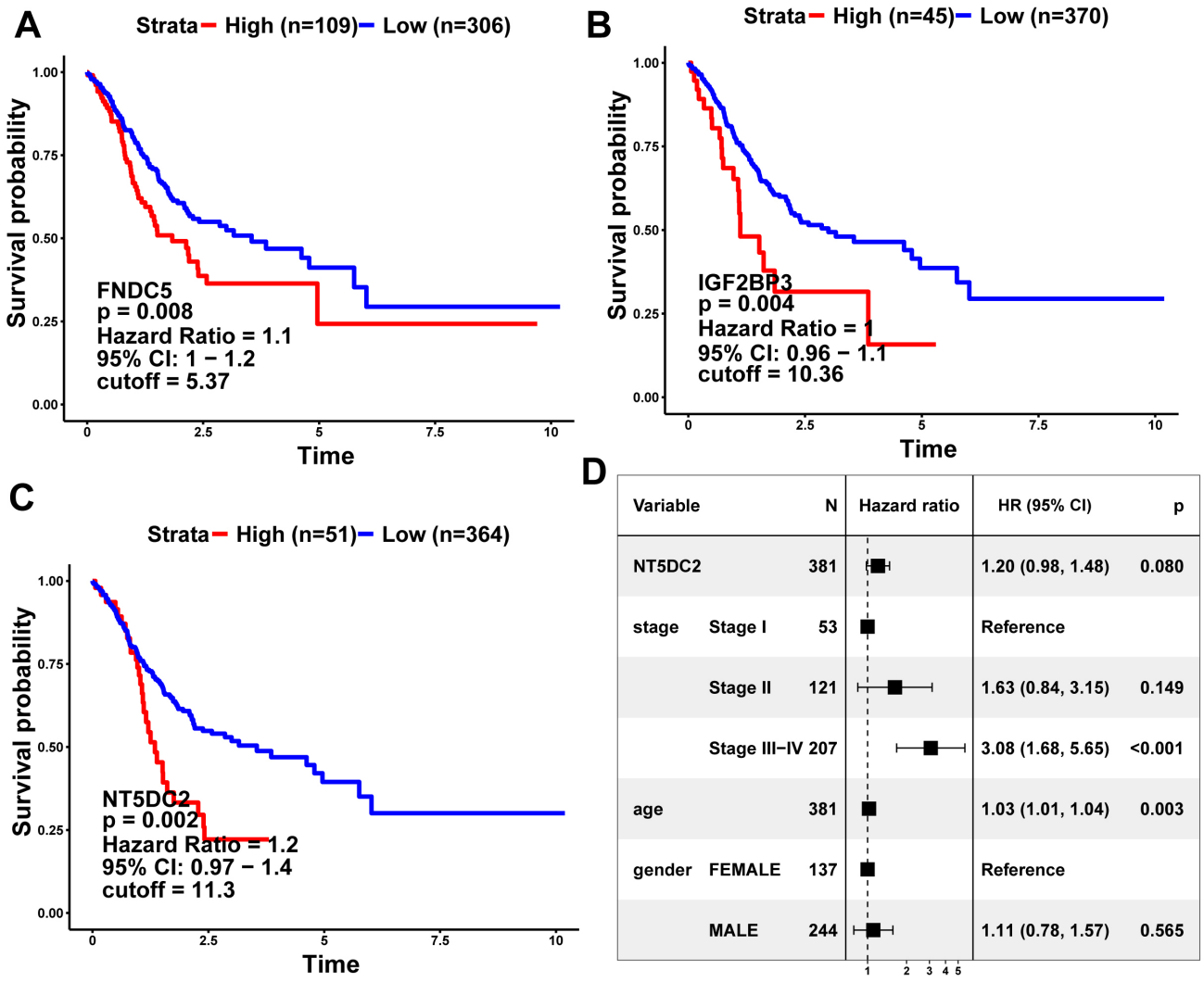

Fig. 4. Construction of the prognostic model. (A–C) OS curves of *FNDC5*, *IGF2BP3*, and *NT5DC2* in TCGA-STAD. (D) HR forest plot of the multivariate Cox regression risk model constructed by combining *NT5DC2* with clinical data. HR, hazard ratio.

Observable expression shifts were visually mild in certain cell groups due to sparse single-cell read coverage.

GSEA Analysis of FNDC5, NT5DC2, and IGF2BP3 in Specific Cells

In this single-patient exploratory dataset, single-cell-level pathway enrichment analysis was performed to explore potential functions of the three genes within distinct cell subsets. Fig. 7A,B displays GSEA results linked to *NT5DC2* expression in tumor epithelial cells. The enrichment patterns implied potential engagement of multiple signaling programs relevant to cellular metabolism and survival. Several gene sets associated with ferroptosis suppression were enriched, including HALLMARK_OXIDATIVE_PHOSPHORYLATION, HALLMARK_MTORC1_SIGNALING, HALLMARK_PROTEIN_SECRETION, HALLMARK_FATTY_ACID_METABOLISM, and HALLMARK_PEROXISOME. These signatures raise the hypothesis that altered energy metabolism, cellular stress tolerance, and lipid homeostasis may contribute to suppressed ferroptosis programs and favor tumor cell survival. Gene sets related to glycolytic metabolism also exhibited enrichment trends, such as HALLMARK_MYC_TARGETS_V1, HALLMARK_MTORC1_SIGNALING, HALLMARK_FATTY_ACID_METABOLISM, HALLMARK_PI3K_AKT_MTOR_SIGNALING, and HALLMARK_GLYCOLYSIS. These pathway patterns suggest potential links between enhanced glucose metabolic signatures and sustained tumor cell proliferation. Taken together, these correlative enrichment observations generate the hypothesis that elevated *NT5DC2* in tumor epithelial cells may coincide with metabolic reprogramming signatures, alongside signatures reflecting altered ferroptosis and glycolysis programs.

Fig. 7C,D presents GSEA enrichment patterns associated with *IGF2BP3* within tumor-infiltrating B

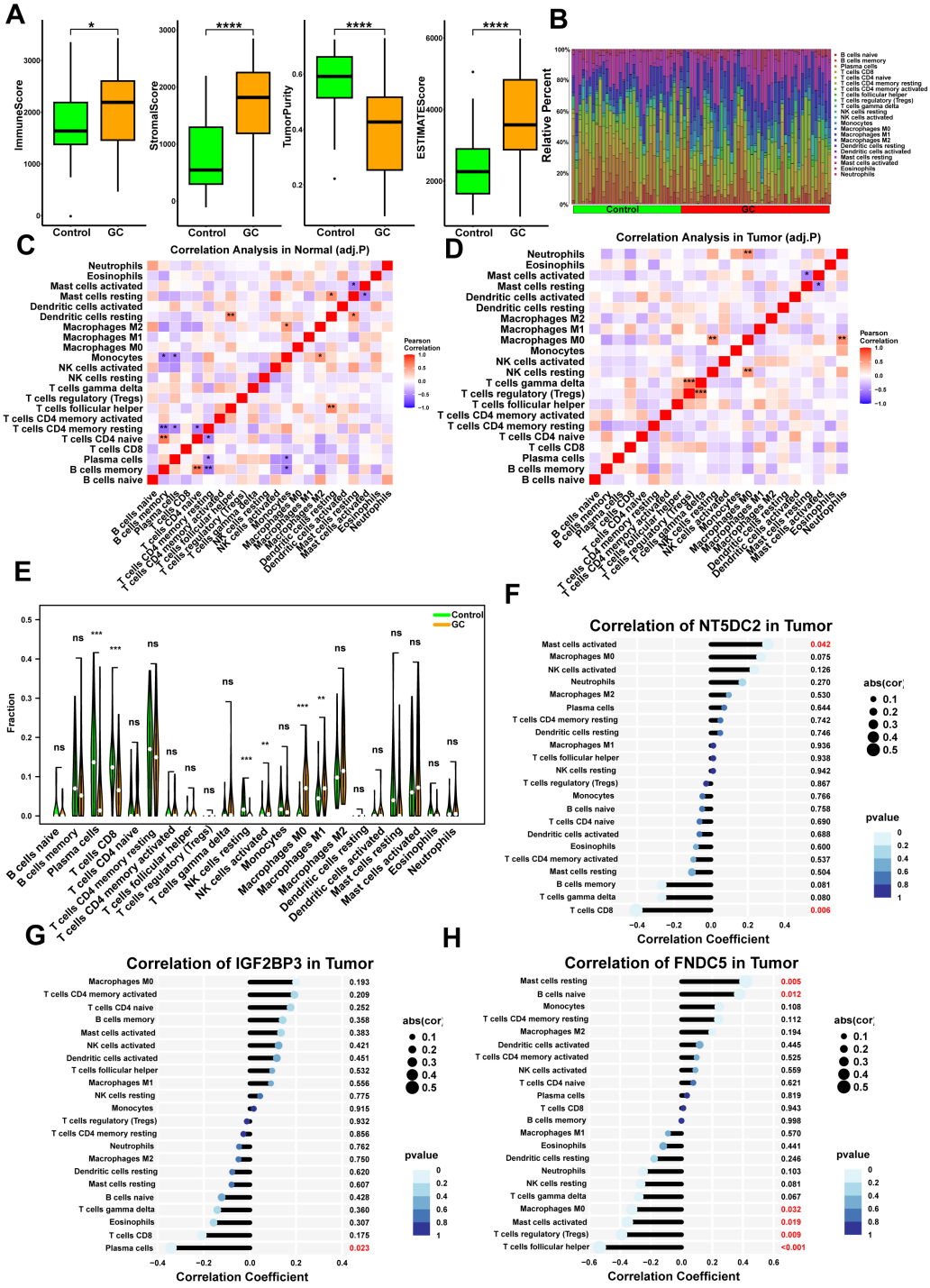

Fig. 5. Immune cell profiles and related analyses in GC samples. (A) Boxplots showing differences in ImmuneScore, ESTIMATEScore, TumorPurity, and StromalScore between normal and GC samples in the experimental set. (B) Relative abundances of immune cell types in each GC sample, represented by distinct colors. (C) Correlation matrix of immune cells in normal patients after TumorPurity adjustment. (D) Correlation matrix of immune cells in tumor patients after TumorPurity adjustment. (E) Comparison of 22 immune cell types between GC samples and healthy controls after TumorPurity adjustment. (F–H) Correlations between 3 key genes (*NT5DC2*, *IGF2BP3*, *FNDC5*) and immune cell infiltration in GC patients. *$p < 0.05$, **$p < 0.01$, ***$p < 0.001$, ****$p < 0.0001$, ns, not significant.

cells. Enriched gene sets linked to high *IGF2BP3* expression could be grouped into two broad functional categories. The first group contained signatures related to glycolysis and ferroptosis regulation, including HALLMARK_MYC_TARGETS_V1, HALLMARK_MTORC1_SIGNALING, HALL-

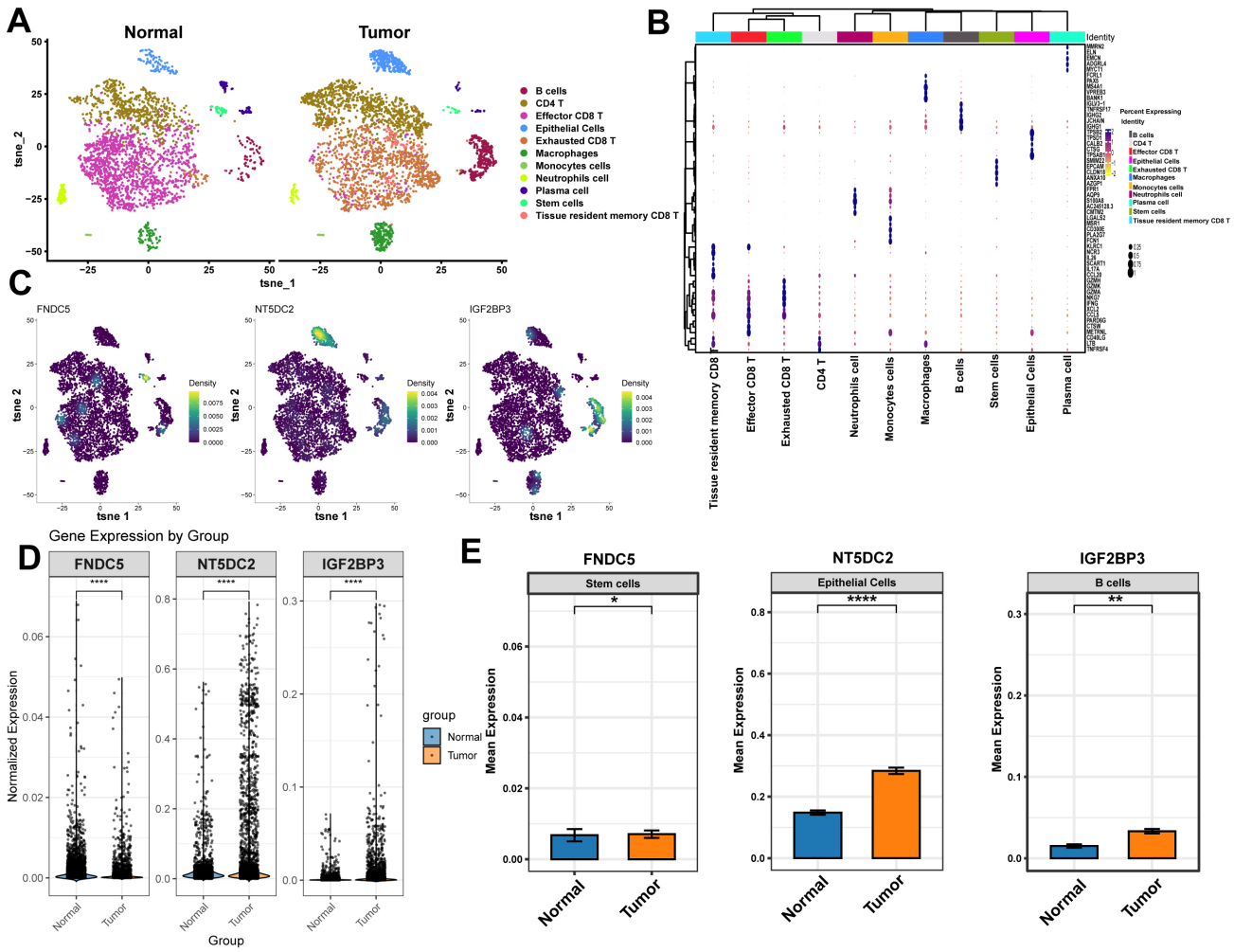

Fig. 6. Expression patterns of FNDC5, NT5DC2, and IGF2BP3 in GC single-cell data. (A) t-SNE plot showing dimensionality reduction of single cells from normal and tumor patients (cell types: B cells, CD4 T cells, Effector CD8 T cells, Epithelial Cells, Exhausted CD8 T cells, Macrophages, Monocytes, Neutrophils, Plasma cells, Stem cells, Tissue resident memory CD8 T cells). (B) Bubble plot of highly variable genes across 11 cell types. (C) Expression density plots of *FNDC5*, *NT5DC2*, and *IGF2BP3* in the t-SNE dimension. (D) Violin plot showing the difference in imputed *FNDC5*, *NT5DC2*, and *IGF2BP3* expression levels between normal and tumor groups (all cells). (E) Bar plot showing the difference in imputed *FNDC5* (in Stem cells), *NT5DC2* (in Epithelial cells), and *IGF2BP3* (in B cells) expression levels between normal and tumor groups. *$p < 0.05$, **$p < 0.01$, ****$p < 0.0001$.

MARK_OXIDATIVE_PHOSPHORYLATION, and HALLMARK_UNFOLDED_PROTEIN_RESPONSE. Within tumor-infiltrating B cells, these pathway signatures hint at potential metabolic adaptation and improved stress tolerance that may support B cell persistence. The second category included gene sets related to genome maintenance and environmental adaptation, such as HALLMARK_DNA_REPAIR and HALLMARK_XENOBIOTIC_METABOLISM. These signatures imply potential mechanisms enabling B cells to withstand apoptotic stimuli and microenvironmental stressors. Given the apparent cell-cell communication trends between tumor epithelial cells and tumor-infiltrating B cells identified via CellChat, these B cell-associated pathway signatures serve as correlative clues for future investigation into tumor progression. Collectively, the pathway enrichment profiles provide exploratory clues that *IGF2BP3* may correlate with altered metabolic and stress response signatures to sustain the viability of tumor-infiltrating B cells.

Gene sets showing enrichment trends linked to *FNDC5* in normal gastric stem cells included mTORC1 signaling, oxidative phosphorylation, MYC target genes, the G2/M checkpoint, DNA repair, and cholesterol homeostasis signatures (Fig. 7E). While these pathways are broadly implicated in cell proliferation and metabolic activation, their coordinated enrichment trends observed in *FNDC5*-high normal gastric stem cells raise a hypothesis of a distinctive homeostatic regulatory profile associated with normal gastric stem cell physiology. Additional path-

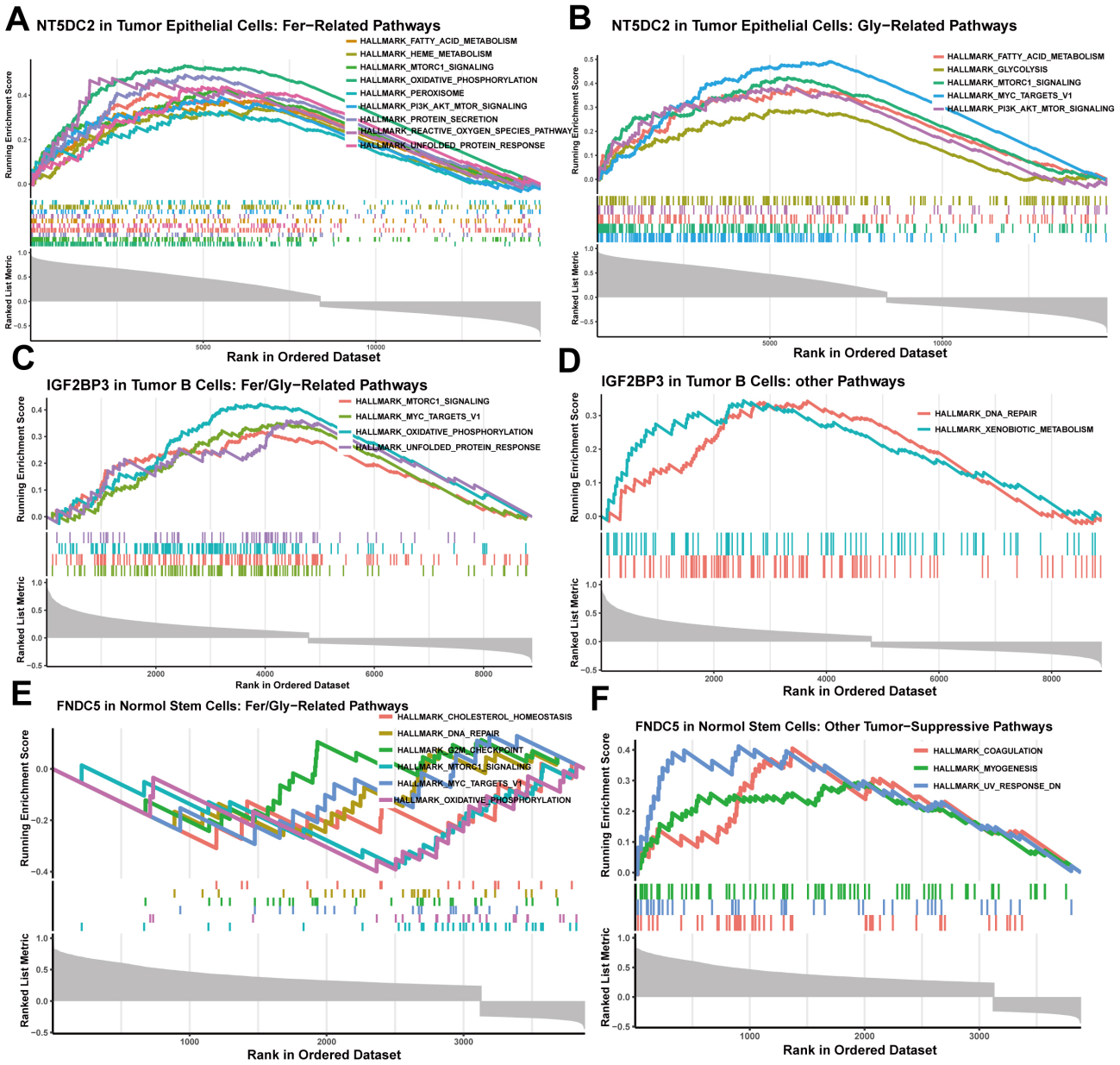

Fig. 7. Gene Set Enrichment Analysis (GSEA) of *NT5DC2*, *IGF2BP3*, and *FNDC5* in single-cell data. (A) GSEA curves of NT5DC2 in Tumor Epithelial Cells: Fer-Related Pathways. (B) GSEA curves of NT5DC2 in Tumor Epithelial Cells: Gly-Related Pathways. (C) GSEA curves of *IGF2BP3* in Tumor B Cells: Fer/Gly-Related Pathways. (D) GSEA curves of *IGF2BP3* in Tumor B Cells: Other Pathways. (E) GSEA curves of FNDC5 in Normal Stem Cells: Fer/Gly-Related Pathway. (F) GSEA curves of *FNDC5* in Normal Stem Cells: Other Tumor-Suppressive Pathways.

way signatures also displayed enrichment trends alongside *FNDC5*, including coagulation, UV response DN, and myogenesis gene sets (Fig. 7F). These functional programs are associated with tissue homeostasis, DNA damage response and cell differentiation. The observed enrichment patterns suggest potential combinative contributions to the steady-state phenotype of normal gastric stem cells in this sample.

Cell Communication Analysis Further Reveals Heterogeneity of Cell Interactions in Normal/GC Patients

In this single-patient exploratory dataset, a cell-cell communication network was constructed based on single-cell transcriptomic profiles to explore divergent cell interaction patterns between normal gastric tissue and GC tissue (**Supplementary Fig. 1A**). In normal tissue, cell populations including plasma cells, monocytes and effector $CD8^+$ T cells displayed active intercellular communication. For

example, plasma cells exhibited frequent communication events with other cell subsets (103 interactions with B cells, 151 interactions with $CD4^+$ T cells, and 159 interactions with effector $CD8^+$ T cells). By comparison, the communication network in GC tissue displayed broader and intensified interaction patterns. Notably, epithelial cells, exhausted $CD8^+$ T cells and B cells showed elevated communication frequency and intensity (e.g., 130 communication links between epithelial cells and effector $CD8^+$ T cells, and 33 links between B cells and exhausted $CD8^+$ T cells). Shell plots (**Supplementary Fig. 1B**) further illustrated a trend of increased signal transmission from epithelial cells toward exhausted $CD8^+$ T cells, alongside elevated communication intensity from B cells to exhausted $CD8^+$ T cells. These observations raise the hypothesis that tumor-associated cell interactions linked to immunosuppressive phenotypes may be augmented within the tumor microenvironment. In addition, module clustering analysis was performed on incoming and outgoing signals in the GC sample (**Supplementary Fig. 1C**). For outgoing signal modules, B cells, epithelial cells and exhausted $CD8^+$ T cells formed independent clusters. Effector $CD8^+$ T cells clustered together with stem cells, whereas monocytes shared a module with neutrophils. Correspondingly, within incoming signal modules, B cells, epithelial cells and exhausted $CD8^+$ T cells still constituted separate clusters. Effector $CD8^+$ T cells clustered with plasma cells, and monocytes remained grouped with neutrophils alongside neutrophils. Two Sankey diagrams further displayed ligand–receptor pairs associated with these modules. These profiles suggest enhanced heterogeneity of cell-cell communication in GC tissue and highlight candidate interaction links between immune cells and tumor epithelial cells for further validation.

Identification of Key Signals for Communication Between Epithelial Cells/B Cells and Exhausted $CD8^+$ T Cells in Tumor Samples

To explore candidate signal crosstalk among epithelial cells, B cells and exhausted $CD8^+$ T cells in GC tissue, signaling patterns of the BMP, TGF-β, EGF and GRN pathways were characterized (**Supplementary Fig. 2**). Signal intensity scatter plots revealed the following trends. The BMP pathway was dominated by epithelial cells and exhausted $CD8^+$ T cells; epithelial cells acted as prominent signal senders, while exhausted $CD8^+$ T cells served as primary signal receivers. In the TGF-β pathway, exhausted $CD8^+$ T cells exhibited high activity for both signal sending and receiving, and epithelial cells also ranked highly among signal receivers. For the EGF pathway, effector $CD8^+$ T cells and epithelial cells constituted major signal sources, and exhausted $CD8^+$ T cells represented the primary receiving population. Within the GRN pathway, epithelial cells and B cells functioned as main signal senders, whereas $CD4^+$ T cells and exhausted $CD8^+$ T cells were predominant receivers. Bubble plots indicated that communication from B cells to exhausted $CD8^+$ T cells relied on the GRN–SORT1 ligand-receptor axis. Interactions originating from epithelial cells toward exhausted $CD8^+$ T cells engaged four pathways (BMP, TGF-β, EGF, GRN) involving 22 ligand-receptor pairs. Among these, interactions including AREG–(EGFR+ERBB2), TGFB1–(TGFBR1+TGFBR2), AREG–EGFR, and TGFB1–(ACVR1+TGFBR1)/TGFB3–(TGFBR1+TGFBR2) appeared most prominent. Expression profiling visualized the distribution of these ligand-receptor pairs across epithelial cells, B cells and exhausted $CD8^+$ T cells. Correlation analyses showed correlative trends whereby epithelial *NT5DC2* exhibited positive correlations with GRN ($r = 0.87$), AREG ($r = 0.57$), and TGFB1 ($r = 0.35$), alongside negative correlations with BMP2 ($r = -0.37$) and BMP4 ($r = -0.36$). These correlative patterns generate the hypothesis that *NT5DC2* may be associated with tumor-related intercellular signaling, potentially amplifying epithelial cell influences on exhausted $CD8^+$ T cells and corresponding signatures linked to immune escape. In B cells, *IGF2BP3* displayed a positive correlation trend with GRN expression. This pattern suggests a candidate linkage between *IGF2BP3* and communication events connecting B cells to exhausted $CD8^+$ T cells.

Construction of an TIDE-Predicted Response Classification Model

To evaluate the potential roles of *FNDC5, NT5DC2*, and *IGF2BP3* in the response to GC immunotherapy, this study first analyzed the correlations between the TIDE index, Interferon Gamma (IFNG), Microsatellite Instability (MSI), $CD8^+$ T score of TCGA-STAD patients, and the expression of the three genes (**Supplementary Fig. 3A**). The overall trend showed that high expression levels of *NT5DC2* and *IGF2BP3* were positively correlated with the TIDE index, and negatively correlated with IFNG, MSI, and $CD8^+$ T score, suggesting that they might inhibit immune response and promote immune escape; the expression of *FNDC5* was positively correlated with both the TIDE index and $CD8^+$ T score, but negatively correlated with IFNG and MSI, indicating that it might have a bidirectional role in immune regulation. Immunotherapy survival analysis (**Supplementary Fig. 3B**) showed that the overall survival of patients who responded to immunotherapy was significantly higher than that of non-responder patients, indicating that this score was consistent with clinical practice. The ROC analysis of single-gene and gene combination models (**Supplementary Fig. 3C**) showed the following results: among the single-gene models, *FNDC5* achieved the highest predictive performance (AUC = 0.724), followed by *NT5DC2* (AUC = 0.611) and *IGF2BP3* (AUC = 0.557); among the two-gene models, the *FNDC5* + *NT5DC2* combination yielded the highest AUC (0.756), followed by *FNDC5* + *IGF2BP3* (0.728) and *NT5DC2* + *IGF2BP3* (0.624). The AUC of the triple-gene combination (*FNDC5* + *NT5DC2* + *IGF2BP3*) reached 0.762, indicating that the

triple-gene combination model had the highest predictive performance. The calibration curve further demonstrated good agreement between the predicted and observed TIDE-predicted responses (**Supplementary Fig. 3D**). To analyze the comprehensive effect of the three genes on TIDE-predicted response, a multivariate logistic regression model (**Supplementary Fig. 3E**) was constructed. The results showed that *FNDC5* (OR = 0.57, 95% CI 0.49–0.67, $p < 0.001$), *NT5DC2* (OR = 0.52, 95% CI 0.38–0.71, $p < 0.001$), and *IGF2BP3* (OR = 0.90, 95% CI 0.82–1.00, $p = 0.043$) were all independent factors affecting TIDE-predicted response, which indicated that the three genes still had independent predictive value in the comprehensive model. In general, high expression levels of *NT5DC2* and *IGF2BP3* might promote immune suppression and escape, whereas the mechanism of *FNDC5* was more complex. Nevertheless, the triple-gene combination could effectively predict the TIDE-predicted response of GC patients.

NT5DC2 Modulates Proliferation, Migration, and Apoptosis in GC Cells

Among the three survival-relevant hub genes (*FNDC5, IGF2BP3, NT5DC2*), *NT5DC2* displayed consistent differential expression trends across all datasets. In addition, *NT5DC2* is specifically expressed in gastric epithelial tumor cells, whereas *FNDC5* and *IGF2BP3* are mainly enriched in stem cells and B cells, respectively, making it more convenient for cellular functional experiments. Therefore, we prioritized *NT5DC2* for subsequent *in vitro* and *in vivo* functional validation to further clarify its biological role in GC progression. As shown in Fig. 8, qPCR and Western blot analyses demonstrated that *NT5DC2* expression was significantly upregulated at both the mRNA and protein levels in the gastric cancer cell line MKN-7 compared with the normal gastric epithelial cell line GES-1 (Fig. 8A,B, $p < 0.05$). *NT5DC2* was subsequently silenced in MKN-7 cells using siRNA, and qPCR analysis confirmed that si2-NT5DC2 achieved the highest knockdown efficiency, which was therefore selected for subsequent functional assays (Fig. 8C, $p < 0.05$). CCK-8 assays revealed that knockdown of *NT5DC2* markedly suppressed the proliferative capacity of MKN-7 cells (Fig. 8D, $p < 0.05$). Consistently, cell migration assays showed that *NT5DC2* silencing significantly attenuated the migratory ability of MKN-7 cells (Fig. 8E, $p < 0.05$). In addition, flow cytometric analysis indicated that depletion of *NT5DC2* significantly increased apoptosis in MKN-7 cells (Fig. 8F, $p < 0.05$). *In vitro* experiments demonstrated that *NT5DC2* was highly expressed in gastric cancer cells. Knockdown of *NT5DC2* reduced cell proliferation and migration while increasing apoptosis.

NT5DC2 Silencing Suppresses Tumor Growth In Vivo

A xenograft model was established using nude mice injected with MKN-7 cells expressing either control (sh-NC) or *NT5DC2*-targeting (sh-NT5DC2) shRNA. *NT5DC2* was subsequently silenced in MKN-7 cells using shRNA. qPCR analysis confirmed that sh-NT5DC2-3 achieved the highest knockdown efficiency; therefore, it was selected for subsequent functional assays (Fig. 9A, $p < 0.05$). Tumors in the sh-NT5DC2 group were smaller in size, weight, and volume than those in the control group (Fig. 9B–D, $p < 0.05$). IHC staining indicated reduced tumor proliferative activity, with decreased expression of Ki67 in sh-NT5DC2 tumors (Fig. 9E, $p < 0.05$). H&E staining confirmed that sh-NC tumors had higher cellular density and more mitotic figures, while sh-NT5DC2 tumors had a more diffuse arrangement with fewer mitotic cells (Fig. 9F).

Discussion

Gastric cancer is often diagnosed at an advanced stage, with a five-year overall age-standardized relative survival rate of 38.3% (2007–2011), 40.6% (2012–2016), and a predicted 42.9% (2017–2021) according to US SEER-based model analysis [19]. Prompt surgical resection is the only potentially curative treatment available at this time; however, outcomes are highly variable by stage. These discrepancies reinforce the importance of developing novel treatment options. Improved outcomes may be achieved through the identification of consistent molecular targets [20]. Immune evasion has emerged as one of the core mechanisms underlying the failure of immunotherapy in GC [21]. Research findings have demonstrated that, in GC patients, reduced $CD8^+$ T cell infiltration, low activity of the IFN-γ signaling pathway, elevated tumor immune suppression indices, and decreased microsatellite instability (MSS/low-MSI status) are closely associated with poor responses to ICIs [22]. In the present study, we confirmed through immune infiltration analysis that GC samples exhibited significantly higher ImmuneScore, StromalScore, and ESTIMATEScore compared with normal tissues, while tumor purity was remarkably decreased. Further analysis revealed that high expression levels of *NT5DC2* and *IGF2BP3* were positively correlated with TIDE and other immune evasion-related indicators. Further correlation analysis revealed that high expression levels of *NT5DC2* and *IGF2BP3* were positively correlated with TIDE and other immune evasion-related indicators. Although *FNDC5* showed complex immune correlations, it retained independent predictive weight in the combined signature. Based solely on bulk and single-cell transcriptome correlation data, we put forward a hypothetical linkage between glycolysis-ferroptosis transcriptional programs and the GC immunosuppressive microenvironment. Notably, this correlative observation cannot be defined as a confirmed regulatory axis without targeted pathway blocking or immune co-culture functional tests.

For the three screened genes, existing literature provides partial evidence linking them to tumor metabolism,

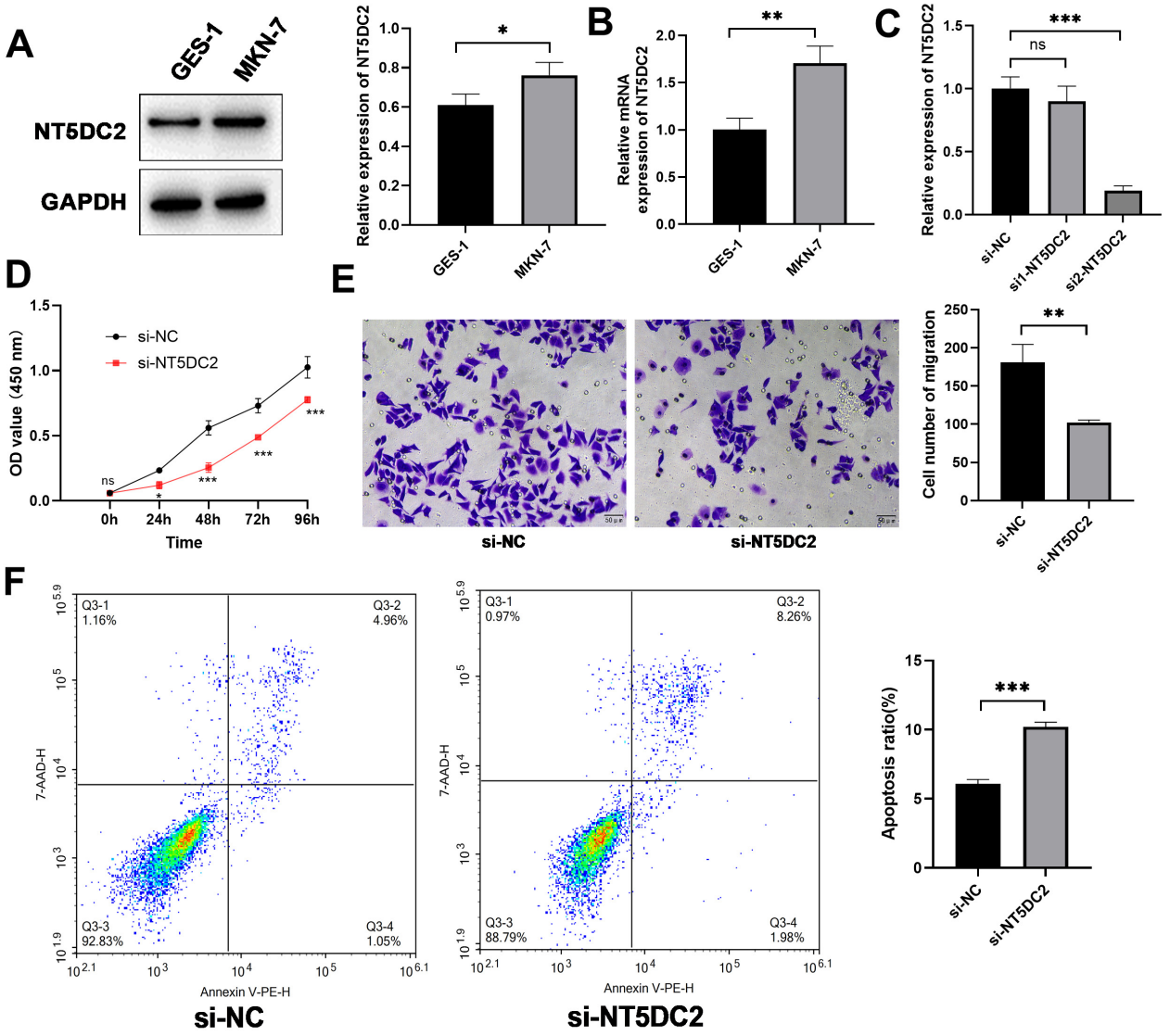

Fig. 8. *NT5DC2* regulates proliferation, migration, and apoptosis in MKN-7 cells. (A,B) *NT5DC2* expression levels in GES-1 and MKN-7 cells were detected by qPCR and Western Blot analyses, respectively. (C) Efficient *NT5DC2* knockdown in MKN-7 cells. (D) *NT5DC2* knockdown reduces cell proliferation. (E) *NT5DC2* knockdown decreases cell migration. (F) *NT5DC2* knockdown increases cell apoptosis. $*p < 0.05$, $**p < 0.01$, $***p < 0.001$, ns, not significant. n = 3 biologically independent replicates for all cellular experiments.

cell fate, and immune regulation: *IGF2BP3*, an mRNA-binding protein, has been reported in multiple studies to stabilize pro-proliferative and metabolism-related mRNAs to promote tumor glycolytic reprogramming and proliferation (linking to invasion and poor prognosis) [23,24]. It can also enhance ferroptosis resistance in colon cancer by stabilizing *SLC7A11* and is regulated by *miR-98-5p* [25]. *NT5DC2*, identified as an oncogenic factor in several tumor types, may regulate cell metabolism and survival through pathways such as EGFR [26]. In this study, its upregulation in epithelial cells was associated with enhanced glycolysis-related pathways and ferroptosis inhibition, supporting the hypothesis that *NT5DC2* participates in metabolic reprogramming of epithelial cells to promote ferroptosis resistance. FNDC5/Irisin has complex functions in different tumor contexts—some studies confirm its protective/differentiation or tumor-suppressive roles (by inhibiting the mTOR pathway and ROS) [27,28,29]. In this study (overall downregulation of *FNDC5* in tumors but worse prognosis in patients with high expression), its "dual regulatory role" involves both glycolysis inhibition and ferroptosis inhibition, where the balance of these functions shifts in different tumor progression stages or cellular contexts (e.g., ferroptosis inhibition outweighs proliferation inhibition in some environments, leading to high expression-associated poor prognosis). Thus, *IGF2BP3* and *NT5DC2*

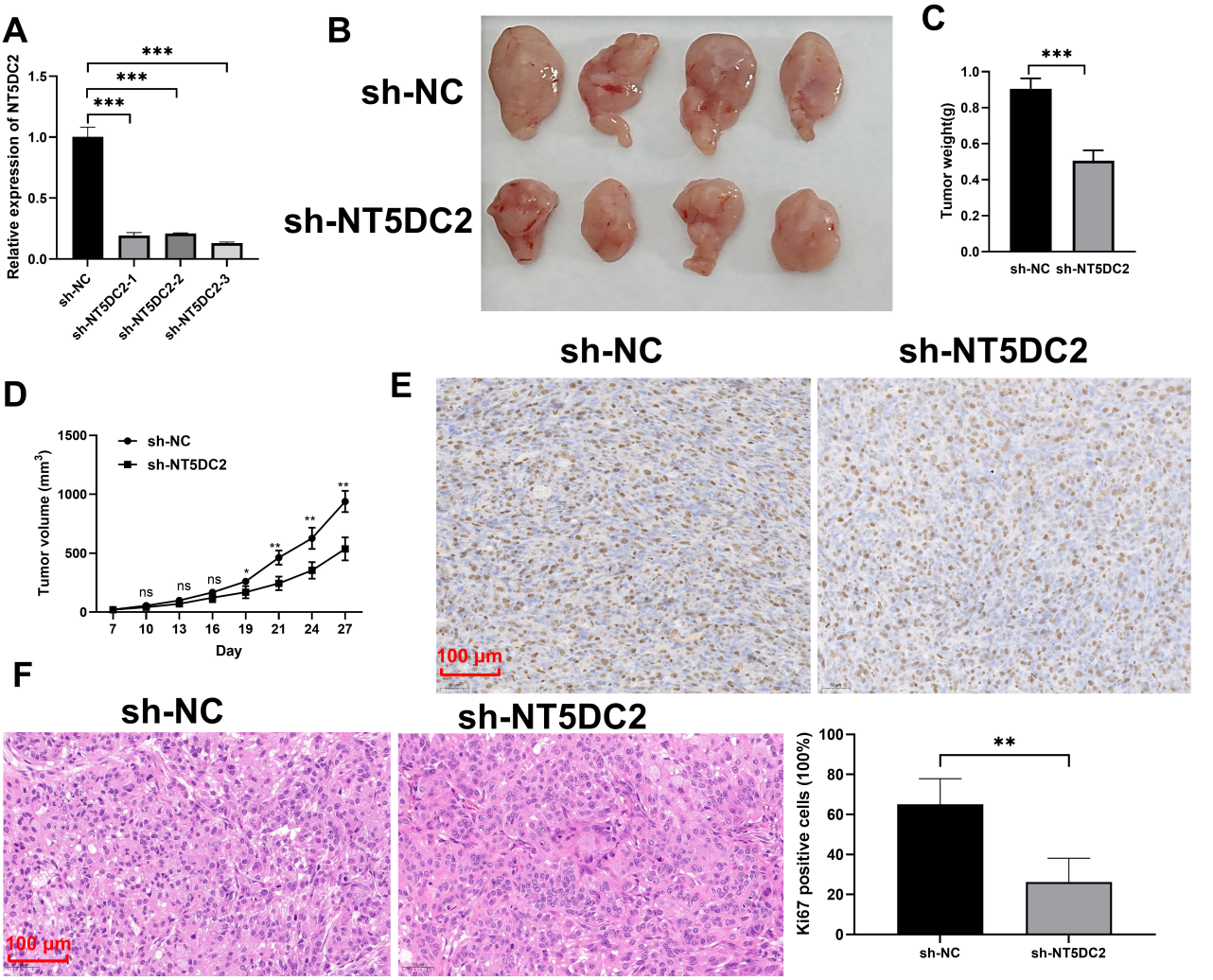

Fig. 9. *NT5DC2* silencing suppresses GC growth *in vivo*. (A) Efficient *NT5DC2* knockdown in MKN-7 cells. (B) Images of heterotopic xenografts. (C,D) Tumor weight and volume of mice from the *NT5DC2* knockdown and sh-NC groups. (E) Ki-67 immunohistochemical staining of tumor sections from the *NT5DC2* knockdown group and sh-NC group (scale bar = 100 μm, magnification 20×). (F) The histopathological changes in subcutaneous tumor tissues were analyzed with Hematoxylin and eosin (H&E) staining (scale bar = 100 μm, magnification 20×). n = 4 biologically independent mice per group. *$p < 0.05$, **$p < 0.01$, ***$p < 0.001$, ns, not significant vs sh-NC.

act as oncogenic molecules that "promote glycolysis and inhibit ferroptosis", while *FNDC5* may show opposite clinical associations in different contexts due to its bidirectional regulatory effect—an explanation consistent with the cell-type-specific expression observed at the single-cell level and GSEA results.

Through single-cell analysis and cell communication network investigation, this study found that in tumor samples, crosstalk between epithelial cells (with high *NT5DC2* expression) and exhausted $CD8^+$ T cells was significantly enhanced via pathways including GRN (progranulin), EGF, TGF-β, and BMP. Evidence shows that TGF-β mediates immunosuppression in the tumor microenvironment (TME) (inducing Tregs, inhibiting effector $CD8^+$ T cell activity and infiltration) [30,31] and correlates with immune checkpoint therapy resistance [32,33]. EGF signaling promotes epithelial/tumor cell proliferation and indirectly facilitates immunosuppression [34,35,36]. GRN and its receptors (e.g., SORT1) drive immunosuppressive phenotypes and treatment resistance [37], while BMP signaling affects myeloid cells, the negative correlation between NT5DC2 and BMP2/4 suggests NT5DC2 does not drive epithelial-to-exhausted $CD8^+$ T cell signaling via BMP upregulation—BMP may instead reflect other cell types (e.g., myeloid cells) status or act as a compensatory/feedback pathway [38,39]. Regarding B cells, the positive correlation between IGF2BP3 and GRN, combined with the finding that B cells mediate the GRN–SORT1 axis towards exhausted $CD8^+$ T cells, suggests that B cells may promote $CD8^+$ T cell exhaustion by secreting GRN or regulating receptor–ligand

pairing, thereby impairing anti-tumor immunity [37,40,41]. Naumnik et al. [42] found B cell-attracting chemokine-1 and GRN in bronchoalveolar lavage fluid of patients with lung cancer. We hypothesize that the two genes may cooperatively reshape an immunosuppressive microenvironment and induce T cell exhaustion by modulating glycolysis and anti-ferroptosis signatures, but the direct causal connection between metabolic reprogramming and immune dysfunction remains unvalidated in our current experimental system. These observations are consistent with the immune infiltration patterns, as well as the correlations between *NT5DC2/IGF2BP3* expression and immunotherapy-related indicators, such as TIDE scores, IFNG expression, and $CD8^+$ T cell levels.

Of note, functional validation in the current research was selectively performed only on *NT5DC2* rather than *IGF2BP3* and *FNDC5*. This selection was mainly based on *NT5DC2*'s predominant epithelial localization, which facilitates *in vitro* cellular experiments and subsequent *in vivo* xenograft assays. Knockdown of *NT5DC2* significantly restrains GC cell proliferation, migration and subcutaneous tumor growth in nude mice. By contrast, *FNDC5* and *IGF2BP3* exert predominant regulatory effects on immune cells and the tumor immune microenvironment, as indicated by our multi-omics analyses. Therefore, functional verification of these two candidates will be addressed in future independent research focusing on immune microenvironment modulation.

Our study was limited by the use of only one GC cell line, which fails to reflect gastric cancer heterogeneity. In addition, although candidate hub genes were identified through bioinformatic enrichment of glycolysis and ferroptosis pathways, rescue experiments or direct biochemical detection of glycolysis and ferroptosis indicators were not performed. Therefore, the regulatory network connecting NT5DC2 to glycolysis/ferroptosis-associated immunosuppressive microenvironment phenotypes remains to be experimentally validated. We rely solely on correlation analysis and CellChat prediction to hypothesize potential links between NT5DC2/IGF2BP3 and CD8+ T cell exhaustion via TGF-β and GRN-mediated intercellular communication, without corresponding co-culture or pathway inhibition verification experiments. Meanwhile, in this single-patient exploratory dataset, CellChat and expression correlations suggested potential signaling relationships that require validation in independent multi-patient cohorts. Furthermore, our TIDE-based response classification signature was only assessed using computationally predicted response status within the TCGA-STAD dataset and lacks external validation in clinical cohorts with real-world immunotherapy outcome data. These mechanistic verifications will be addressed in future independent investigations.

Conclusion

Glycolysis- and ferroptosis-related genes were analyzed in gastric cancer, identifying *FNDC5*, *NT5DC2*, and *IGF2BP3* as candidate hub genes. Integrated analyses of bulk and single-cell transcriptomic data, immune profiling and cell–cell communication analyses support a hypothetical model in which *NT5DC2* and *IGF2BP3* may correlate with immune-related signatures alongside altered glycolysis and ferroptosis pathway programs. Nevertheless, our study lacks direct functional experiments to validate this metabolic-immune regulatory cascade. A signature built upon these genes exhibited exploratory capacity to stratify patients according to TIDE-predicted immunotherapy response. Functional assays indicated that *NT5DC2* knockdown reduced proliferation and migration, increased apoptosis in MKN-7 cells, and also suppressed tumor growth in a subcutaneous xenograft model.

Availability of Data and Materials

The data analyzed in this study was obtained from the Gene Expression Omnibus (GEO) database (https://www.ncbi.nlm.nih.gov/geo/), including datasets GSE65801, GSE118916, GSE54129, GSE118897, and GSE146996. The gene expression data and clinical data of TCGA-STAD were retrieved from the Xena Browser (https://xenabrowser.net/datapages/). Experimental data used or analyzed during the current study are available from the corresponding author upon reasonable request.

Author Contributions

YTL and JMC designed the research study. YTL and XZ performed the research. JMC and YFM analyzed the data. YTL drafted the article. All authors contributed to important editorial changes in the manuscript. All authors read and approved the final manuscript. All authors have participated sufficiently in the work and agreed to be accountable for all aspects of the work.

Ethics Approval and Consent to Participate

The animal experiments received approval from the Ethics Committee of Zibo Central Hospital (Approval No. 202211008). All procedures complied with the ARRIVE Guidelines 2.0.

Acknowledgment

Not applicable.

Funding

This work was supported by the Natural Science Foundation of Shandong Province [ZR2022MC174].

Conflict of Interest

The authors declare no conflict of interest.

Supplementary Material

Supplementary material associated with this article can be found, in the online version, at https://doi.org/10.24976/Discov.Med.202638211.202.

References

[1] Ferlay J, Colombet M, Soerjomataram I, Mathers C, Parkin DM, Piñeros M, et al. Estimating the global cancer incidence and mortality in 2018: GLOBOCAN sources and methods. International Journal of Cancer. 2019; 144: 1941–1953. https://doi.org/10.1002/ijc.31937

[2] Shah MA, Kennedy EB, Deighton D, Jhawer M, Kadakia KC, Mukherjee S, et al. Immunotherapy and Targeted Therapy for Advanced Gastroesophageal Cancer: ASCO Guideline Update. Journal of Clinical Oncology:Official Journal of the American Society of Clinical Oncology. 2026; 44: 1145–1165. https://doi.org/10.1200/JCO-25-02958

[3] Takahari D, Ito S, Mizusawa J, Katayama H, Terashima M, Sasako M, et al. Long-term outcomes of preoperative docetaxel with cisplatin plus S-1 therapy for gastric cancer with extensive nodal metastasis (JCOG1002). Gastric Cancer:Official Journal of the International Gastric Cancer Association and the Japanese Gastric Cancer Association. 2020; 23: 293–299. https://doi.org/10.1007/s10120-019-01007-w

[4] Kierans SJ, Kennedy C, Turner R, Flood D, DeMichele E, Wallace M, et al. HIF-1α drives distinct aspects of hypoxia-induced glucose metabolism in intestinal epithelial cells. The Journal of Biological Chemistry. 2026; 302: 113193. https://doi.org/10.1016/j.jbc.2026.113193

[5] Wen J, Zhou S, Peng Y, Chen J, Lai M, Tang S, et al. Hypoxia-driven HIF-1α-dependent glycolysis/lactate-associated signaling promotes autophagy-associated scleral remodeling in experimental myopia. Experimental Eye Research. 2026; 270: 111092. https://doi.org/10.1016/j.exer.2026.111092

[6] Yuan H, Leng W, Yu N, Yu Y, Yang C, Bai Y, et al. Activation of Sirt1 by Glyasperin F Suppresses PI3K/Akt/HIF-1α Signaling and Inhibits Glycolytic Metabolism to Ameliorate Pathology in Rheumatoid Arthritis-Associated Interstitial Lung Disease. FASEB Journal: Official Publication of the Federation of American Societies for Experimental Biology. 2026; 40: e71725. https://doi.org/10.1096/fj.202503559RR

[7] Wang G, Li S, Li F, Zhang Z. Bone Marrow Mesenchymal Stem Cells Inhibit Ferroptosis Through Mitochondrial Transfer and Improve Endothelial Cell Dysfunction. Discovery Medicine. 2025; 37: 1372–1384. https://doi.org/10.24976/Discov.Med.202537198.119

[8] Yu X, Li Y, Zhang Y, Yin K, Chen X, Zhu X. Leonurine Ameliorates Diabetic Nephropathy through GPX4-Mediated Ferroptosis of Endothelial Cells. Frontiers in Bioscience (Landmark Edition). 2024; 29: 270. https://doi.org/10.31083/j.fbl2907270

[9] Cai X, Zheng X, Mao J, Wang Z, Zhuang Y, Shen M, et al. Research Progress of Traditional Chinese Medicine in Regulating Ferroptosis Related to Digestive System Tumors. The American Journal of Chinese Medicine. 2026; 54: 445–482. https://doi.org/10.1142/S0192415X26500163

[10] Chen W, Han L, Wang J, Song L. Ferroptosis: The dawn of reversing drug resistance in digestive cancers. Genes & Diseases. 2025; 13: 101873. https://doi.org/10.1016/j.gendis.2025.101873

[11] Jin X, Zhu H, Chen X, Yang Y, Song D. RON receptor tyrosine kinase regulates glycolysis through MAPK/CREB signaling to affect ferroptosis and chemotherapy sensitivity of thyroid cancer cells. Molecular Medicine Reports. 2024; 30: 234. https://doi.org/10.3892/mmr.2024.13359

[12] Li X, Yang Y, Zhang B, Lin X, Fu X, An Y, et al. Lactate metabolism in human health and disease. Signal Transduction and Targeted Therapy. 2022; 7: 305. https://doi.org/10.1038/s41392-022-01151-3

[13] McLane LM, Abdel-Hakeem MS, Wherry EJ. CD8 T Cell Exhaustion During Chronic Viral Infection and Cancer. Annual Review of Immunology. 2019; 37: 457–495. https://doi.org/10.1146/annurev-immunol-041015-055318

[14] Bautista J, López-Cortés A. T cell exhaustion landscapes and therapeutic modulation in cancer immunity. Frontiers in Cell and Developmental Biology. 2026; 14: 1827716. https://doi.org/10.3389/fcell.2026.1827716

[15] Shimasaki N. Manufacturing strategies for prolonged CAR-T cell persistence. Cytotherapy. 2026; 28: 102778. https://doi.org/10.1016/j.jcyt.2026.102778

[16] Yu K, Gu Y, Zhang P, Fang H, Cao Y, Wang J, et al. Intratumoral PD-1^{+}CD8^{+} T cells associate poor clinical outcomes and adjuvant chemotherapeutic benefit in gastric cancer. British Journal of Cancer. 2022; 127: 1709–1717. https://doi.org/10.1038/s41416-022-01939-8

[17] Triantafillidis JK, Konstadoulakis MM, Papalois AE. Immunotherapy of gastric cancer: Present status and future perspectives. World Journal of Gastroenterology. 2024; 30: 779–793. https://doi.org/10.3748/wjg.v30.i8.779

[18] Seyed Jafari SM, Hunger RE. IHC Optical Density Score: A New Practical Method for Quantitative Immunohistochemistry Image Analysis. Applied Immunohistochemistry & Molecular Morphology:AIMM. 2017; 25: e12–e13. https://doi.org/10.1097/PAI.0000000000000370

[19] Li Y, Feng A, Zheng S, Chen C, Lyu J. Recent Estimates and Predictions of 5-Year Survival in Patients with Gastric Cancer: A Model-Based Period Analysis. Cancer Control:Journal of the Moffitt Cancer Center. 2022; 29: 10732748221099227. https://doi.org/10.1177/10732748221099227

[20] Liu Y, Xiao Y, Chen Y, Meng E, Jin M, Wu M, et al. Advances in Integrated Radionuclide Diagnosis and Therapy for Gastric Cancer: Targets, Tracers and Translational Applications. World Journal of Gastroenterology, Hepatology and Endoscopy. 2026; 31: 1–16.

[21] Tufail M, Jiang CH, Li N. Immune evasion in cancer: mechanisms and cutting-edge therapeutic approaches. Signal Transduction and Targeted Therapy. 2025; 10: 227. https://doi.org/10.1038/s41392-025-02280-1

[22] Yan SY, Fan JG. Application of immune checkpoint inhibitors and microsatellite instability in gastric cancer. World Journal of Gastroenterology. 2024; 30: 2734–2739. https://doi.org/10.3748/wjg.v30.i21.2734

[23] Xu Z, Pei C, Cheng H, Song K, Yang J, Li Y, et al. Comprehensive analysis of FOXM1 immune infiltrates, m6a, glycolysis and ceRNA network in human hepatocellular carcinoma. Frontiers in Immunology. 2023; 14: 1138524. https://doi.org/10.3389/fimmu.2023.1138524

[24] Sharma G, Gutierrez M, Jones AE, Jaiswal AK, Neeb ZT, Rios A, et al. Metabolic regulation of RNA methylation by the m(6)A-reader IGF2BP3. bioRxiv. 2024. (preprint)

[25] Sun Y, Liu Q, Wu J, Jiang G, Shi H, Zhang Y, et al. IGF2BP3 enhances ferroptosis resistance in colon cancer by stabilizing SLC7A11 and is regulated by miR-98-5p. Frontiers in Oncology. 2025; 15: 1576895. https://doi.org/10.3389/fonc.2025.1576895

[26] Sang R, Yu X, Xia H, Qian X, Yong J, Xu Y, et al. NT5DC2 knockdown suppresses progression, glycolysis, and neuropathic

pain in triple-negative breast cancer by blocking the EGFR pathway. Molecular Carcinogenesis. 2024; 63: 785–796. https://doi.org/10.1002/mc.23688

[27] Kumar M, Sengar AS, Lye A, Kumar P, Mukherjee S, Kumar D, et al. FNDC5/irisin mitigates the cardiotoxic impacts of cancer chemotherapeutics by modulating ROS-dependent and -independent mechanisms. Redox Biology. 2025; 80: 103527. https://doi.org/10.1016/j.redox.2025.103527

[28] Zhao F, Xu D, Wang X, Wang X. FNDC5 affects invasion and migration of oral cancer by inhibiting PI3K/Akt/Snail signaling pathway. Scientific Reports. 2024; 14: 26881. https://doi.org/10.1038/s41598-024-78391-6

[29] Zhu T, Zhang W, Zhang Y, Lu E, Liu H, Liu X, et al. Irisin/FNDC5 inhibits the epithelial-mesenchymal transition of epithelial ovarian cancer cells via the PI3K/Akt pathway. Archives of Gynecology and Obstetrics. 2022; 306: 841–850. https://doi.org/10.1007/s00404-022-06427-1

[30] Batlle E, Massagué J. Transforming Growth Factor-β Signaling in Immunity and Cancer. Immunity. 2019; 50: 924–940. https://doi.org/10.1016/j.immuni.2019.03.024

[31] Lainé A, Labiad O, Hernandez-Vargas H, This S, Sanlaville A, Léon S, et al. Regulatory T cells promote cancer immune-escape through integrin αvβ8-mediated TGF-β activation. Nature Communications. 2021; 12: 6228. https://doi.org/10.1038/s41467-021-26352-2

[32] Niu M, Yi M, Wu Y, Lyu L, He Q, Yang R, et al. Synergistic efficacy of simultaneous anti-TGF-β/VEGF bispecific antibody and PD-1 blockade in cancer therapy. Journal of Hematology & Oncology. 2023; 16: 94. https://doi.org/10.1186/s13045-023-01487-5

[33] Wu Q, You L, Nepovimova E, Heger Z, Wu W, Kuca K, et al. Hypoxia-inducible factors: master regulators of hypoxic tumor immune escape. Journal of Hematology & Oncology. 2022; 15: 77. https://doi.org/10.1186/s13045-022-01292-6

[34] Chen X, Gao A, Zhang F, Yang Z, Wang S, Fang Y, et al. ILT4 inhibition prevents TAM- and dysfunctional T cell-mediated immunosuppression and enhances the efficacy of anti-PD-L1 therapy in NSCLC with EGFR activation. Theranostics. 2021; 11: 3392–3416. https://doi.org/10.7150/thno.52435

[35] Pinte S, Delfortrie S, Havet C, Villain G, Mattot V, Soncin F. EGF repeats of epidermal growth factor-like domain 7 promote endothelial cell activation and tumor escape from the immune system. Oncology Reports. 2022; 47: 8. https://doi.org/10.3892/or.2021.8219

[36] Xin H, Zhong Y, Zhang M, Wu L, Li Q, Li X, et al. An Immune Model Incorporating NK Cells and IL-12 to Predict the Efficacy of the Initial Treatment Cycle of Efgartigimod in Generalized Myasthenia Gravis. Drug Design, Development and Therapy. 2026; 20: 598742. https://doi.org/10.2147/DDDT.S598742

[37] Li J, Huang W, Kuang J, Zhou S, Li Y, Xia Y. Integrated multiomics analysis highlights the immunosuppressive role of granulin precursor positive macrophages in hepatocellular carcinoma. PeerJ. 2025; 13: e18879. https://doi.org/10.7717/peerj.18879

[38] Ihle CL, Straign DM, Canari JA, Torkko KC, Zolman KL, Smith EE, et al. Unique macrophage phenotypes activated by BMP signaling in breast cancer bone metastases. JCI Insight. 2024; 9: e168517. https://doi.org/10.1172/jci.insight.168517

[39] Saadey AA, Yousif A, Osborne N, Shahinfar R, Chen YL, Laster B, et al. Rebalancing TGFβ1/BMP signals in exhausted T cells unlocks responsiveness to immune checkpoint blockade therapy. Nature Immunology. 2023; 24: 280–294. https://doi.org/10.1038/s41590-022-01384-y

[40] Cheung PF, Yang J, Fang R, Borgers A, Krengel K, Stoffel A, et al. Progranulin mediates immune evasion of pancreatic ductal adenocarcinoma through regulation of MHCI expression. Nature Communications. 2022; 13: 156. https://doi.org/10.1038/s41467-021-27088-9

[41] Qi Q, Cai X, Lv Q. Charting the immune terrain: a novel risk model for thyroid cancer prognosis. Frontiers in Genetics. 2026; 17: 1752017. https://doi.org/10.3389/fgene.2026.1752017

[42] Naumnik W, Panek B, Ossolińska M, Naumnik B. B Cell-Attracting Chemokine-1 and Progranulin in Bronchoalveolar Lavage Fluid of Patients with Advanced Non-small Cell Lung Cancer: New Prognostic Factors. Advances in Experimental Medicine and Biology. 2019; 1150: 11–16. https://doi.org/10.1007/5584_2018_285